

1

2 **Convective Momentum Transport Associated with the Madden-Julian**
3 **Oscillation Based on a Reanalysis Dataset**

4

5 Ji-Hyun Oh, Xianan Jiang, Duane E. Waliser

6 *Joint Institute for Regional Earth System & Engineering/UCLA, Los Angeles, CA*
7 *Jet Propulsion Laboratory, California Institute of Technology, Pasadena, CA*

8

9 Mitchell W. Moncrieff

10 *National Center for Atmospheric Research, Boulder, CO*

11

12 Richard H. Johnson

13 *Colorado State University, Fort Collins, CO*

14

15

16

17

18 Submitted to *J. Climate* 08/2014

19 Revised 03/2015

20

21

22

23

24 *Corresponding author address:* Dr. Xianan Jiang, Jet Propulsion Laboratory, California Institute of
25 Technology, MS 233-300, 4800 Oak Grove Drive, Pasadena, CA 91109. Email: xianan@ucla.edu.

26 Copyright © 2014. All rights reserved.

Abstract

27

28

29

30

31

32

33

34

35

36

37

38

39

40

41

42

43

44

45

46

Better understanding of multi-scale interactions within the Madden-Julian Oscillation (MJO), including the momentum exchanges, is critical for improved MJO prediction skill. In this study, convective momentum transport (CMT) associated with the MJO is analyzed based on the NOAA Climate Forecast System Reanalysis (CFSR). A three-layer vertical structure associated with the MJO, as previously suggested in the mesoscale momentum tendency profile based on global cloud resolving model simulations, is evident in the subgrid momentum tendency from the CFSR. Positive (negative) subgrid momentum tendency anomalies are found near the surface, negative (positive) anomalies in the low-to-mid troposphere, and positive (negative) anomalies in upper troposphere are found within and to the west (east) of the MJO convection. This tends to damp the MJO circulation in the free atmosphere, while enhancing MJO winds near the surface. In addition, it could also reduce the MJO eastward propagation speed and lead to the backward tilt with height in the observed MJO structure through a secondary circulation near the MJO center. Further analyses illustrate that this three-layer vertical structure in subgrid momentum tendency largely balances the grid-scale u-momentum transport, mainly through the transport of seasonal mean u-wind by the MJO-scale vertical motion. Synoptic-scale systems, which were proposed to be essential for the u-momentum transport of the MJO previously, however, are found to play a minor role for the total grid-scale momentum tendency. The above momentum tendency structure is also confirmed with the ECMWF analysis for the period of the Year of the Tropical Convection (YOTC), which lends confidence to these above results based on the CFSR.

47 **1. Introduction**

48 As one of the most pronounced modes of tropical climate variability, the Madden-Julian
49 Oscillation (MJO; Madden and Julian 1971, 1994) plays a critical role in bridging global weather
50 and climate, and serves as one of primary predictability sources for extended-range forecasts (Lau
51 and Waliser 2012; Zhang 2005). The MJO is often initiated over the western equatorial Indian
52 Ocean (IO) and propagates eastward along the equator at a phase speed of about 5 m s^{-1} . Exhibiting
53 a planetary spatial scale of about 5,000–10,000 km, the MJO is characterized by organization of a
54 hierarchy of multi-scale convective systems (Moncrieff et al. 2012). The slowly eastward migrating
55 MJO envelope contains embedded fast eastward moving super cloud clusters (SCC) with horizontal
56 scales of several thousand kilometers, which in turn comprise smaller westward-moving cloud
57 clusters (Nakazawa 1988; Takayabu 1994; Roundy 2008; Kiladis et al. 2009). The SCCs have been
58 identified as the convectively coupled Kelvin waves (Nakazawa 1988; Takayabu and Murakami
59 1991; Takaya and Nakamura 2001), and the westward-moving cloud clusters as the westward
60 inertia-gravity waves, or so-called “two-day waves” (Chen et al. 1996; Takayabu et al. 1996).
61 These convectively coupled waves (CCWs) further consist of scattered cumulus clouds and
62 organized mesoscale convective systems (MCSs) or squall-lines.

63 In spite of the recent great efforts toward improving the ability of general circulation models
64 (GCMs) to simulate the MJO, significant challenges still remain for current GCMs to produce more
65 realistic MJO simulations (Slingo et al. 1996; Lin et al. 2006; Kim et al. 2009; Hung et al. 2013;
66 Jiang et al. 2015). There is a general consensus that large deficiencies in current GCMs in
67 representing the MJO could be primarily due to our lack of understanding the interactions between
68 the MJO and embedded multi-scale convective systems (e.g., Majda 2007; Moncrieff 2010;
69 Moncrieff et al. 2012; Zhang et al. 2013). The importance in depicting the multi-scale convection
70 organization of the MJO is further supported by improvement of MJO simulations in recent global

71 cloud-system resolving models (Miura et al. 2007) and super-parameterized GCMs (Benedict and
72 Randall 2009). On one hand, dynamical (e.g., vertical wind shear, convergence) and thermo-
73 dynamical (moisture, instability) conditions associated with the MJO can exert significant
74 modulations on the activity of CCWs and MCSs; on the other hand, these small-scale convective
75 systems can feed back to the MJO through significant upscale transport of moisture, heating, and
76 momentum (e.g., Houze 1973; Houze et al. 2000; Houze 2004; Majda and Biello 2004; Khouider et
77 al. 2012b; Majda and Stechmann 2014). While most of previous studies have focused on collective
78 impacts of multi-scale convective systems on thermodynamic properties of the MJO, recent limited
79 observational studies and idealized modeling work have suggested that convective momentum
80 transport (CMT) by smaller convective systems could also play a critical role for the observed MJO
81 structure (see recent reviews by Majda and Stechmann 2011, 2014).

82 It is generally considered that unorganized cumulus convection tends to damp the large-scale
83 flow as a frictional process, i.e., acts downscale to the environmental vertical wind shear (Majda
84 and Stechmann 2008; Khouider et al. 2012b). In contrast, organized MCSs and convectively
85 coupled waves (CCWs) can have either upgradient (amplifying) or downgradient (weakening)
86 effects on the large-scale winds as a direct effect of the vertical tilt of the associated circulation
87 (Moncrieff 1992; Moncrieff and Klinker 1997, hereafter MK97; Majda and Stechmann 2009).
88 Backward vertical tilting structures of convective systems relative to their propagation direction
89 have been widely observed (Mapes et al. 2006; Kiladis et al. 2009), with scales ranging from
90 mesoscale (MCSs), synoptic scale (CCWs), to planetary scales (MJO). Moreover, GCM studies
91 suggest that representation of mean climate (Kim et al. 2008; Richter and Rasch 2008; Song et al.
92 2008) as well as the MJO (Wu et al. 2007; Deng and Wu 2010; Zhou et al. 2012;) is significantly
93 improved by including the CMT effects in climate models. Thus, there has been increasing interest

94 in exploring the CMT associated with these multi-scale convective systems, particularly its role in
95 the evolution of the MJO circulation, which is the focus of this study.

96 By conducting a residual budget analysis on the momentum equation, Tung and Yanai (Tung
97 and Yanai 2002a, b) analyzed evolution of CMT profiles associated with the two major MJO events
98 over the equatorial western Pacific (WP) during the Tropical Ocean Global Atmosphere Coupled
99 Ocean-Atmosphere Response Experiment (TOGA COARE; Webster and Lukas 1992). During the
100 westerly onset phase of the MJO, it was suggested that kinetic energy is transferred upscale from
101 subgrid systems to the large-scale zonal flow, thus helping to enhance the MJO low-level westerly
102 winds (Tung and Yanai 2002a). After the low-level westerly winds fully developed (MJO westerly
103 wind burst phase), however, the CMT largely acts as a friction by decelerating the large-scale zonal
104 flow and reducing the zonal wind shear. By using radar data during the same TOGA COARE
105 period and focusing on the CMT induced by mesoscale super convective systems, Houze et al.
106 (2000) identified strong mid-level inflow associated with mesoscale downdraft in MCSs. In the
107 MJO westerly onset region, this mesoscale inflow transports easterly momentum downward, thus
108 reducing the westerlies near the surface; while in the strong westerly region, the mesoscale inflow
109 jets bring westerly momentum downward, accelerating the westerly wind burst of the MJO. These
110 interesting observational findings motivated many follow-up investigations on the role of CMT for
111 the MJO (e.g., Majda and Stechmann 2008; 2009; Wang and Liu 2011; Khouider et al. 2012a;
112 Miyakawa et al. 2012), most of which were based on a simplified theoretical framework.

113 The multi-scale organization of tropical convection is very difficult to realistically represent in
114 current climate models due to model deficiencies in parameterizing the moist convection and
115 insufficient horizontal resolution to adequately resolve MCSs and even CCWs. Therefore, a so-
116 called “multi-cloud model” approach has been recently employed to study interactions between
117 multi-scale tropical convection and the large-scale environment (Khouider and Majda 2006b, a,

118 2007, 2008b; Khouider and Majda 2008a). The concept of a multi-cloud model is mainly based on
119 a representation of transition between three different cloud types, namely, congestus, deep
120 convective, and stratiform clouds as observed during the evolution of tropical convection (Lin and
121 Johnson 1996; Johnson et al. 1999; Kikuchi and Takayabu 2004; Jiang et al. 2011; Del Genio et al.
122 2012). Significant improvement of the MJO simulations was also achieved by implanting the multi-
123 cloud model in global GCMs (Khouider et al. 2011; Ajayamohan et al. 2013). Based on the multi-
124 cloud model framework, Majda and Stechmann (2009) demonstrated that a two-way interaction
125 between large-scale circulation and CCW activity can lead to oscillation of the large-scale flow on
126 an intraseasonal time scale. By neglecting the Coriolis force, propagation of CCWs in this model is
127 controlled by advection of large-scale flow. Due to its westward tilt with height in the circulation,
128 the Kelvin-wave-like eastward CCWs tend to enhance lower-level large-scale westerly winds. The
129 increased vertical zonal wind shear, however, tends to damp the eastward propagating CCWs
130 themselves while favoring the westward inertial-gravity (WIG) wave-like CCWs. As a result, the
131 prevalence of the westward propagating CCWs leads to the reduction of low-level westerlies, and
132 restores an environment favorable for eastward CCWs. Henceforth, the oscillation in the large-scale
133 circulation continues.

134 This two-way interaction between the large-scale circulation and CCWs critically relies on the
135 way that CCWs respond to changes in the environmental flow. Modulation of Kelvin and WIG-like
136 CCWs by the vertical wind shear as illustrated by Majda and Stechmann (2009) was further
137 confirmed by experiments based on a similar multi-cloud model but on a beta-plane (Han and
138 Khouider 2010; Khouider et al. 2012b). In particular, MJO modulation of convective activity was
139 examined in detail in Khouider et al. (2012b) by specifying observed background wind shear and
140 moisture profiles during different MJO phases in the model. It was suggested that Kelvin waves are
141 most favored to the east of MJO convection where strong westerly vertical wind shear (easterlies at

142 low-level, westerlies at upper-level) prevails, which is expected to decelerate the MJO circulation.
143 Meanwhile, largely fed by the environmental moisture, MCSs or squall-line systems tend to be
144 prominent in the convectively active region near the MJO center. Moving along the low-level
145 environmental flow, the CMT induced by these organized MCSs might play a role in accelerating
146 the MJO circulation on both sides of the MJO center as also suggested in other studies (Majda and
147 Stechmann 2008; Khouider et al. 2012a). To the west of the MJO center away from the core active
148 region, picked by the strong easterly wind shear, the WIG waves are most active and tend to damp
149 the large-scale winds.

150 By considering a Kelvin (WIG) wave on the west (east) side of the MJO convection, Wang
151 and Liu (2011) examined the CMT impact from the CCWs on the instability and propagation of the
152 MJO based on a $2^{1/2}$ -layer intermediate model (Wang and Li 1994). While the CMT effect itself by
153 Kelvin and WIG waves under this configuration did not contribute to the propagation of the MJO
154 mode in this model, inclusion of the CMT impact in addition to the frictional-CISK (convective
155 instability of the second kind) can lead to a more realistic growth rate and propagation speed of the
156 model MJO. This result, however, is highly sensitive to the preference of CCW activity relative to
157 the MJO. While prescription of the WIG wave to the east of the MJO in Wang and Liu (2011) was
158 largely motivated by the observational analysis in Kikuchi and Wang (2010) for a limited period of
159 the summer of 1990, enhanced WIG wave activity to the east of the MJO differs from the multi-
160 cloud model results mentioned above. In general, how CCW activity is modulated by the MJO in
161 the reality is not yet fully understood, and has not been comprehensively characterized based on
162 available observations.

163 Recently, Miyakawa et al. (2012) quantitatively analyzed CMT profiles associated with the
164 MJO based on output from a global 7-km cloud-system resolving model (CRM), the
165 Nonhydrostatic Icosahedral Atmospheric Model (NICAM; Satoh et al. 2008), for a period of 32

166 days from 15 December 2006 which mainly covered one MJO event as reported in Miura et al.
167 (2007). It was illustrated that the mesoscale convection-induced CMT in zonal wind component
168 exhibits the largest amplitude to the west of the MJO center with a well-defined three-layer vertical
169 structure: positive u-momentum tendency near the surface, negative from the lower- to mid-
170 troposphere, and positive in the upper troposphere. It was proposed that this mesoscale CMT effect
171 could be partially responsible for the vertical tilt in the observed MJO structure, delay the eastward
172 progress of the low- to mid- troposphere westerly wind and thus reduce the MJO propagation
173 speed.

174 Despite the accumulating evidence on its significant role for the MJO as suggested by
175 previous studies, our understanding of CMT processes remains limited. In particular, previous
176 results in characterizing the CMT of the MJO based on the TOGA COARE field campaign and
177 CRM simulations involve just a few MJO events with a limited focus over the WP. Additionally,
178 although theoretical studies with simplified assumptions have provided great insight into the multi-
179 scale interactions associated with the MJO through CMT, they necessitate observational
180 verification.

181 In this study, we analyze characteristics of the CMT related to the MJO over the IO and WP,
182 mainly using a relatively long-term (12 years) and high-resolution (50km) state-of-the-art reanalysis
183 dataset generated by a GCM that parameterizes the CMT due to subgrid processes (“subgrid-scale”
184 CMT hereafter). Note that the terminology of “CMT” in this study is intended to represent
185 momentum transports either directly through parcel updrafts and downdrafts in scattered cumuli or
186 MCSs, or eddy momentum transports through organized circulation associated with MCSs or
187 CCWs where local convective signal may not be explicitly evident. This paper is structured as
188 follows. Datasets and approaches used for the analysis are described in Section 2. In Section 3,
189 detailed structure of momentum transport associated with the MJO by both subgrid and resolved-

190 scale processes based on the reanalyses are examined. A summary and discussion are presented in
191 Section 4.

192 **2. Data and methods**

193 **2a. Data**

194 The dataset mainly used for this study is the Climate Forecast System Reanalysis (CFSR; Saha
195 et al. 2010) from the National Centers for Environmental Prediction (NCEP). The CFSR is
196 generated by the NCEP Global Forecast System (GFS) atmospheric model, at a global horizontal
197 resolution of T382 (~38 km) with 64 native vertical levels, coupled to the Geophysical Fluid
198 Dynamics Laboratory (GFDL) Modular Ocean Model (MOM) version 4. The GFS takes into
199 account the CMT using a simplified Arakawa-Schubert cumulus scheme by allowing both updraft
200 and downdraft mass fluxes to transport momentum (Arakawa and Schubert 1974; Pan and Wu
201 1995; Moorthi et al. 2001). The CFSR dataset used for this study was archived at a $0.5^\circ \times 0.5^\circ$
202 spatial resolution with 37 pressure levels, and at a 6-hourly temporal interval.

203 The European Centre for Medium-Range Forecasts (ECMWF) analysis data for the two-year
204 period of May 2008–April 2010 during the Year of Tropical Convection (YOTC; Moncrieff et al.
205 2012; Waliser et al. 2012; hereafter EC-YOTC dataset) were also utilized to provide an independent
206 validation of the CMT features of the MJO as revealed in the CFSR. The EC-YOTC dataset used in
207 this study has a $0.5^\circ \times 0.5^\circ$ spatial resolution, 25 pressure levels, and a 6-hourly temporal resolution.

208 Additionally, 3-hourly TRMM 3B42 (version 7; Huffman et al. 1995) rainfall data are also
209 employed to assess the fidelity of the CFSR to represent the MJO. The TRMM data are derived
210 from the combination of high quality microwave estimates calibrated with infrared (IR) estimates
211 and rain gauge analyses. The dataset covers 50°S to 50°N with a 0.25° longitude-latitude spatial
212 resolution at a 3-hourly time interval.

213 This study focuses on the wintertime (November-April) when the MJO exhibits its strongest
214 variability. The CFSR and TRMM rain rates are analyzed for 12 winters from 1998 to 2010, and
215 EC-YOTC is examined for two winters from 2008 to 2010. Since the MJO circulation is dominated
216 by the zonal wind, our primary focus in this study is confined to the role of CMT by various spatial
217 / temporal scales on the zonal momentum budget of the MJO.

218

219 **2b. Methods**

220 The tendency equation for the zonal wind on a model grid in pressure coordinates can be
221 written as follows

$$222 \quad \frac{\partial u}{\partial t} = -u \frac{\partial u}{\partial x} - v \frac{\partial u}{\partial y} - \omega \frac{\partial u}{\partial p} + f(y)v - \frac{\partial \varphi}{\partial x} + X \quad (1)$$

223 where u and v are zonal and meridional winds, respectively, ω the vertical pressure velocity, f the
224 Coriolis parameter, and φ geopotential height. X is the time rate of change of the zonal wind
225 (acceleration/deceleration) due to unresolved physical subgrid-scale processes, including the CMT,
226 vertical diffusion, and gravity-wave drag, etc, as well as a non-physical increment term induced at
227 each reanalysis cycle. By employing a residual momentum budget analysis approach, previous
228 studies suggested that CMT could be the most dominant subgrid-scale process in the free
229 troposphere over the tropical oceans (Carr and Bretherton 2001; Tung and Yanai 2002b; Lin et al.
230 2005). However, accurate estimates of the subgrid CMT term by using the residual budget analysis
231 greatly suffers from large uncertainties in several reanalysis fields including the vertical velocity
232 and geopotential height, which do not have direct observational constraints, as well as the
233 reanalysis incremental term, that often can be comparable to physical terms in amplitude (e.g.,
234 Kiranmayi and Maloney 2011; Mapes and Bacmeister 2012). Hence, in this study, instead of using
235 a residual budget analysis for the momentum, we take advantage of the parameterized CMT fields
236 archived from both CFSR and EC-YOTC reanalyses to represent the subgrid-scale CMT.

237 In general, the subgrid cumulus effect on environmental momentum can be represented as
238 below following Shapiro and Stevens (1980),

$$239 \quad \frac{\partial \vec{V}}{\partial t} = -M_c \frac{\partial \vec{V}}{\partial p} + \delta(\vec{V}_c - \vec{V}) + \sigma \left(\frac{1}{\rho} \nabla p^* \right) \quad (2)$$

240 where \vec{V} represents the environmental (grid-scale) wind, \vec{V}_c the wind in the cloud, M_c the cloud
241 mass flux, δ the mass detrainment at the cloud boundaries, p^* the convection-induced pressure
242 perturbation, and σ the fractional area covered by cumulus clouds. The first term on the right side
243 represents the environmental momentum field through the part of environmental vertical motion
244 compensating convective mass flux, which depends on the environmental wind shear and
245 magnitude of the convective mass flux. The second term stands for the detrainment of excess
246 momentum from clouds, and the third term for the convection-induced pressure gradient force. All
247 these three CMT effects were considered in the version of the GFS model used for the CFSR with
248 the third effect being taken into account by empirically increasing the entrainment for momentum
249 in the updraft (Moorthi et al. 2001). A similar treatment of subgrid CMT was also adopted in the
250 Cy31r1 version of the ECMWF model that was used for the EC-YOTC analysis¹.

251 In order to quantify the significance of the subgrid-scale CMT associated with the MJO with
252 respect to the momentum transport at model grid scales, we examine the advection terms on the
253 right side of Eq. (1). Additionally, the contribution by mesoscale systems to the total grid-scale
254 CMT is also assessed following an approach by Miyakawa et al. (2012). For this purpose, the total
255 variable (u) is assumed to be decomposed into “large-scale” (\bar{u}) and “mesoscale” (u'), e.g., $u =$
256 $\bar{u} + u'$. The large-scale circulation component is derived by the horizontal averaged value within a
257 5° radius of circular area, while the mesoscale circulation at each grid point is obtained by the
258 deviation from the circular mean. Following Miyakawa et al. (2012), a radius of 5° of circular areas

¹ <http://old.ecmwf.int/research/ifsdocs/CY31r1/index.html>

259 was chosen so that it is large enough and that the stratiform along with convective regions
 260 accompanied by MCSs can be captured as the vertical redistribution of momentum by an MCS that
 261 is closely related to the stratiform region (Yang and Houze 1996; Houze 2004). Sensitivity tests
 262 were conducted by slightly changing the radius from 3° to 7° for the scale separation, but results did
 263 not change significantly.

264 The total grid-scale advection terms on the r.h.s. of Eq. (1), which consist of zonal,
 265 meridional, and vertical components, can be further partitioned into²

$$266 \quad -\frac{\partial uu}{\partial x} \approx -\frac{\partial \bar{u}\bar{u}}{\partial x} - \frac{\partial u' u'}{\partial x} \quad (3)$$

$$267 \quad -\frac{\partial uv}{\partial y} \approx -\frac{\partial \bar{u}\bar{v}}{\partial y} - \frac{\partial u' v'}{\partial y} \quad (4)$$

$$268 \quad -\frac{\partial u\omega}{\partial p} \approx -\frac{\partial \bar{u}\bar{\omega}}{\partial p} - \frac{\partial u' \omega'}{\partial p} \quad (5)$$

269 The first terms on the r.h.s. are the large-scale momentum tendency, and the second terms
 270 mesoscale momentum tendency. Several previous studies have suggested that eddy horizontal
 271 momentum transport terms are much smaller than the eddy vertical transport (Carr and Bretherton
 272 2001; Tung and Yanai 2002a, b; Lin et al. 2008), which is also to be shown in the following for the
 273 mesoscale momentum tendency.

274 The Real-Time Multivariate MJO (RMM) index by Wheeler and Hendon (2004) is adopted
 275 for the MJO-cycle composite analysis. The RMM index is derived by the empirical orthogonal
 276 function (EOF) analysis of combined fields of equatorially averaged 850hPa and 200hPa zonal
 277 winds, and outgoing long-wave radiation (OLR). The pair of two leading principal component time
 278 series, i.e., RMM1 and RMM2, defines a two-dimensional phase space of the MJO, and each phase
 279 approximately indicates the location of the MJO convection within its life cycle. MJO life cycle

² On the spatial/temporal scale of the MJO, correlations between a large-scale quantity and a meso-scale quantity are small in general.

280 composites can then be obtained by averaging a given variable over each of eight MJO phases in
281 which the amplitude of the MJO (defined as $\sqrt{RMM_1^2 + RMM_2^2}$ is greater than unity.

282

283 **3. Results**

284 **3a. Vertical subgrid CMT structure associated with the MJO**

285 Before examining detailed CMT structure associated with the MJO, the fidelity of the CFSR
286 in representing the MJO is first illustrated by comparing the MJO life-cycle composite of
287 precipitation based on the CFSR against that by the TRMM observations (Fig. 1). Prior to
288 compositing, daily rainfall fields are first derived based on the 6-hourly CFSR and the 3-hourly
289 TRMM datasets, and are then subjected to band-pass filtering to retain periods of 20–90 days after
290 removal of the climatological annual cycle. For the MJO life-cycle composite based on 12 winters
291 from 1998-2010, there are about 172 strong MJO days on average for each MJO phase. The
292 composite evolution patterns of anomalous rainfall during the eight MJO phases based on TRMM
293 (Fig. 1a) clearly illustrate the origin of the MJO convection over the western IO and its eastward
294 propagation. Although slightly weaker amplitudes in rainfall anomalies are noted in the CFSR
295 composite (Fig. 1b), the eastward propagation as well as the observed phase speed of the MJO is
296 well represented in the CFSR rainfall field, which suggests that the CFSR captures convection
297 signals associated with the MJO quite well. Since CFSR rainfall is consistent with many other
298 variables generated from the reanalysis model, particularly the CMT fields as the focus of this
299 study, in the following we will mainly use CFSR rainfall data to derive an MJO index to
300 characterize the vertical CMT structure associated with the MJO.

301 A linear regression approach is used to derive vertical profiles of various fields related to the
302 MJO. Similar results can be obtained if a composite analysis is applied to these fields based on
303 selected strong MJO events. For regression calculations, MJO indices over the IO and WP are

304 defined by domain averaged 20-90-day band-pass filtered rainfall anomalies over the IO (75°E–
305 85°E, 5°S–5°N) and WP (150°E–160°E, 5°S–5°N), and normalized by their corresponding standard
306 deviations, respectively. Then, the 3D structures associated with the MJO over the IO and WP are
307 derived based on linear regressions between the time series of different 3D variables (predictand)
308 and the corresponding MJO indices (predictor).

309 Figure 2 depicts daily averaged subgrid-scale CMT (shaded) along with 20–90 day band-pass
310 filtered wind (vectors for u and $-v$) and rainfall anomalies (green line with right axis) based on the
311 CFSR reanalysis, by regressing against the IO (a) and WP (b) MJO indices. A baroclinic structure
312 in anomalous wind fields associated with the MJO is clearly evident over both the IO and WP, with
313 westerly (easterly) wind anomalies to the west (east) of the convective center in the lower
314 troposphere, and a reversed circulation at the upper level. In the CMT fields associated with the
315 MJO over the IO, a three-layer structure in subgrid-scale momentum tendency (shaded; Fig. 2a),
316 with a positive sign in the upper troposphere (300-100hPa), a negative center in the mid-
317 troposphere (700-300hPa), and another positive center below 700hPa although rather weak, is
318 evident under and west of the MJO convection center (west of 100°E). A three-layer structure in
319 momentum tendency but with an opposite sign is also noted to the east of 100°E in Fig. 2a. Similar
320 vertical profiles in subgrid-scale momentum tendency corresponding to enhanced MJO convection
321 can also be discerned over the WP (Fig. 2b), although the amplitude in momentum tendency to the
322 east of the convection is rather weak compared to its IO counterpart.

323 Figure 3 further illustrates horizontal distributions of the regressed subgrid-scale anomalous
324 momentum tendency patterns onto the IO (left panels) and WP (right panels) MJO indices at
325 200hPa, 500hPa, and 900hPa, respectively. Also superimposed on these plots are the corresponding
326 regressed rainfall anomalies by green contours. A three-layer structure in subgrid-scale momentum
327 tendency is again readily seen in regression patterns based on both the IO and WP rainfall indices.

328 When the enhanced MJO is located over the IO, positive momentum tendency anomalies over
329 200hPa are slightly shifted to the west side of the enhanced MJO envelope, while negative
330 momentum tendency prevails over a large area to the east and on both sides of enhanced MJO away
331 from the equator (Fig. 3a).

332 On the first order approximation, the u-momentum tendency induced by subgrid-scale CMT
333 as illustrated in Fig. 2 will damp the MJO circulation in the free atmosphere above 700hPa, since
334 low-to-mid-level negative (positive) momentum tendency to the west (east) of the MJO convection
335 center will reduce the westerly (easterly) anomalous winds associated with the MJO; similarly, in
336 the upper-troposphere, positive (negative) momentum tendency to the west (east) side of the MJO
337 center is also against the MJO circulation. However, the lowest branch of the three-layer
338 momentum tendency structure between the surface and 700hPa, namely, positive (negative)
339 momentum tendencies to the west (east), enhance the MJO circulation, particularly, over the WP
340 (Fig. 2b). Since the sustenance of tropical deep convection largely relies on moisture convergence
341 in the planetary boundary layer (PBL) and lower troposphere (Sherwood 1999), the momentum
342 tendency structure due to the sub-grid cumulus effect as suggested in Fig. 2 could exert important
343 influences on the MJO by affecting the coupling between circulation and convection, e.g., the gross
344 moist stability (Neelin and Held 1987; Raymond et al. 2009).

345 On the other hand, as illustrated by Figs. 2 and 3, the strongest anomalous CMT signals in
346 both the middle (~500hPa, negative sign) and upper (~200hPa, positive sign) troposphere are
347 largely collocated with the MJO convection center. This u-momentum tendency will induce an east-
348 west asymmetric divergence tendency relative to the MJO convection center. A similar regression
349 pattern against the IO MJO rainfall index as in Fig. 2a, but for the longitude-height cross-section of
350 zonal convergence of the subgrid-scale momentum tendency, is displayed in Fig. 4a. Additionally,
351 the horizontal divergence patterns of the subgrid-scale u-momentum tendency at different vertical

352 levels are displayed in Fig. 4b-d. It is clearly shown that a maximum divergence (convergence)
353 tendency is located about 10° east (west) of the convection center in the lower-mid-troposphere,
354 with an opposite sign in the upper-levels, suggesting a tendency in generating a secondary
355 circulation in the free troposphere with downward (upward) motion to the east (west) of the MJO
356 center. This tendency in divergence and associated secondary circulation by the subgrid-scale
357 momentum tendency near the MJO center could act as a drag on the eastward propagation of the
358 MJO, which is in accord with previous GCM studies that inclusion of CMT effects in a GCM will
359 reduce the eastward phase speed of the MJO in the model (e.g., Deng and Wu 2010). On the other
360 hand, the divergence tendency in the PBL due to subgrid processes shows a convergence
361 (divergence) tendency to the east (west) of the MJO center (Fig. 4d). As a result, this tendency in
362 generating upward (downward) motion to the east (west) of the MJO could enhance the eastward
363 propagation of the MJO in the PBL, therefore possibly contributing to the vertical tilt structure of
364 the MJO to some degree, although the observed vertical tilting structure of the MJO might be
365 ascribed to multi-cloud development during MJO evolution (e.g., Majda and Biello 2004; Mapes et
366 al. 2006). It is of particular interest to note that this three-layer structure in the subgrid-scale
367 momentum tendencies corresponding to MJO convection over both IO and WP in Fig. 2 closely
368 resemble the composite mesoscale momentum tendency profiles based on CRM simulations in
369 Miyakawa et al. (2012). Since composite analysis was conducted relative to MJO convection over
370 the WP in Miyakawa et al. (2012), the CMT effects were mainly found to the west of the
371 convection center, which is also the case in our regressed CMT pattern over the WP (Fig. 2b). The
372 amplitude of the subgrid-scale momentum tendencies associated with the MJO is also comparable
373 to that of mesoscale tendencies based on CRM simulations. Similar effects by the mesoscale CMT
374 as mentioned above were also discussed in Miyakawa et al. (2012).

375 **3b. Grid-scale momentum transport associated with the MJO**

376 In this subsection, momentum transport associated with the MJO due to grid-scale circulation
377 based on the CFSR reanalysis is examined. One particular question we address is the effects of
378 synoptic-scale waves on the MJO momentum budget compared to that by the subgrid-scale
379 processes examined in the previous section. While we are well aware that organized mesoscale
380 circulations with a scale of hundreds of kilometers (e.g., Houze 2004) are only marginally resolved
381 (“permitted”) by the 50km CFSR data, vertical CMT profiles of u-momentum due to mesoscale
382 systems are explored following the spatial filtering approach utilized by Miyakawa et al. (2012) as
383 previously described. Total u-momentum tendencies associated with the MJO due to grid-scale
384 advection terms in Eq. (1) can then be separated into mesoscale and the remaining large-scale
385 components as in Eqs. (3-5).

386 To demonstrate how the mesoscale spatial filtering approach works, Figure 5 illustrates a map
387 of the standard deviations (STDs) of the mesoscale rainfall. Due to the 50km resolution of CFSR
388 data, the mesoscale rain subject to the spatial filtering will largely represent very large-scale MCSs
389 as well as some small synoptic systems. It should also be mentioned that the scale-separation based
390 on the 5°-radius circular average, while useful, is somewhat arbitrary because the MCSs have no
391 natural cutoff size (Yuan and Houze 2010). Nevertheless, the spatial distribution of the mesoscale
392 rain variability shown in Fig. 5 largely captures major MCS activity centers as revealed by remote-
393 sensing observations (e.g., Schumacher and Houze 2003; Yuan and Houze 2010). For example, the
394 largest STDs of mesoscale rainfall over the Maritime Continent and adjacent oceans are likely
395 associated with a vigorous diurnal cycle of convection and associated propagating gravity waves
396 (Yang and Slingo 2001; Rauniyar and Walsh 2011). Meanwhile, strong MCS activity occurs over
397 the WP along the intertropical convergence zone (ITCZ) and South Pacific convergence zone
398 (SPCZ), consistent with MCSs identified by Yuan and Houze (2010) based on satellite estimates.

399 Therefore, it is reasonable to apply the spatial filtering to isolate MCS systems from the large-scale
400 environment. Similar spatial separation approach is then applied to horizontal wind and vertical
401 velocity fields. Vertical profiles of momentum transport associated with the MJO due to MCSs as
402 well as the remaining large-scale circulation are calculated based on Eqs. (3-5).

403 Figure 6 displays longitude-pressure plots of vertical u-momentum transport by total grid-
404 scale circulation (top), and its separation into mesoscale (middle) and remaining large-scale
405 (bottom) components corresponding to Eq. (5). Note that these vertical profiles are also derived by
406 regression against the IO (left panels) and WP (right panels) MJO indices. In the total vertical grid-
407 scale u-momentum transport fields, the three-layer vertical structure as previously noted in the
408 subgrid-scale momentum tendency is again clearly evident in both regressed patterns over the IO
409 (Fig. 6a) and WP (Fig. 6d), but with *an opposite sign*. To the west (east) of the MJO center,
410 negative (positive) momentum tendency anomalies are present in the upper-level, positive
411 (negative) anomalies at the mid-level, and negative (positive) anomalies again in the lower
412 troposphere, with a comparable magnitude to that of the subgrid-scale tendency. Additionally, very
413 similar to that in the subgrid-scale momentum tendency profile (Fig. 2b), the total grid-scale
414 tendency pattern over the WP exhibits a strong amplitude to the west of the MJO center, in contrast
415 to the rather weak amplitude on the east side (Fig. 6d). The decomposition of the total grid-scale
416 vertical u-momentum transport suggests that the amplitude of the mesoscale vertical CMT transport
417 is comparatively very weak (note the different coloring scales for the two middle panels); namely,
418 the total grid-scale vertical u-momentum transport is dominated by the large-scale transport. The
419 rather weak mesoscale momentum tendency compared to the total grid-scale tendency is not
420 unexpected due to the relatively coarse spatial (50km) and temporal (6-hourly) resolutions of the
421 CFSR that cannot adequately resolve mesoscale systems. Regardless of its weak amplitude,
422 however, a similar three-layer vertical pattern is also evident in the mesoscale momentum tendency

423 profiles (Fig. 6b and 6e), resembling the subgrid-scale CMT structure shown in Fig. 2, and also in
424 agreement with the mesoscale momentum tendency profiles based on CRM simulations in
425 Miyakawa et al. (2012).

426 A comparison of vertical profiles in u-momentum transport by total grid-scale, large-scale,
427 and mesoscale circulations over the IO is further provided in Fig. 7. In addition to the vertical u-
428 momentum transport associated with the MJO (red curves), vertical profiles of zonal (black) and
429 meridional (blue) transport of u-momentum (ref. Eqs. 3-5) are also shown in Fig. 7. Again,
430 compared to the large-scale vertical u-momentum transport, the amplitude of the mesoscale
431 momentum tendency is rather weak; the total grid-scale tendency is mainly contributed by the
432 large-scale transport for both horizontal and vertical transport. Further shown in Fig. 7c is that zonal
433 and meridional components of mesoscale u-momentum transport are weak compared to the vertical
434 mesoscale CMT component. This is consistent with the result of Miyakawa et al. (2012) as well as
435 previous subgrid-scale CMT estimates based on reanalysis datasets (e.g., Carr and Bretherton 2001;
436 Tung and Yanai 2002a, b). In contrast, for the large-scale u-momentum transport (Fig. 7b), both
437 zonal (black) and meridional (blue) transports exhibit comparable amplitude to the vertical
438 component, particularly in the upper troposphere between 300hPa and 100hPa. Both large-scale
439 horizontal transport components tend to counteract the vertical transport. This is also largely
440 consistent with CRM results in Miyakawa et al. (2012; their Fig. 13). Similar results are found in
441 regressed u-momentum transport profiles over the WP (not shown).

442 To further substantiate the results based on the CFSR reanalysis, we analyzed the EC-YOTC
443 reanalysis following the same approach applied to the CFSR. Figure 8 displays longitude-pressure
444 cross-section profiles of momentum tendency by subgrid-scale (Fig. 8a), mesoscale (Fig. 8b), large-
445 scale (Fig. 8c), and total grid-scale vertical transports (Fig. 8d), respectively, based on the EC-
446 YOTC data. Albeit differences are discernible between these two datasets, particularly in the

447 subgrid CMT profiles, which are possibly due to relatively short sampling of the EC-YOTC data as
448 well as differences in deriving the cloud mass fluxes in these two reanalysis models, the vertical
449 CMT structure corresponding to each component derived by EC-YOTC exhibits great similarity to
450 the CFSR results, including the three-layer vertical structure of the momentum tendencies, the
451 opposite sign of the subgrid and grid-scale tendencies, and the dominance of the large-scale
452 contribution to the total grid-scale tendency. This remarkable similarity lends further confidence to
453 the CMT patterns associated with MJO derived from the CFSR reanalysis.

454 **3c. Role of different time scales on the total large-scale momentum transport**

455 Roles of different temporal scales on the total large-scale vertical u-momentum transport
456 profiles of the MJO are further analyzed based on the CFSR reanalysis in this subsection. We
457 decompose the remaining large-scale $[\bar{u}]$ and $[\bar{\omega}]$ fields, subsequent to the removal of mesoscale
458 circulations from the total grid-scale fields, into four different time scales; namely, 2–12 days
459 (synoptic band), 13–20 days (high-frequency intraseasonal band), 21–90 days (intraseasonal band),
460 and beyond 91 days (winter mean state) by applying a Lanczos band-pass filter (Duchon 1979). The
461 vertical profiles of the resultant 16 terms of large-scale vertical u-momentum
462 transport, $-\partial[\bar{u}][\bar{\omega}]/\partial p$, through different combinations of time-filtered $[\bar{u}]$ and $[\bar{\omega}]$, are shown in
463 Fig. 9a and 9b for both the IO and WP. The cutoff frequencies for each variable are denoted in the
464 legend of Fig. 9. It is noteworthy that these different time scale bands as isolated by the band-pass
465 filtering could not be completely exclusive from each other due to slight overlap in the tails
466 between neighboring bands. Sensitivity tests suggest that results will not be significantly changed
467 by using a different band-pass filtering method or by adopting slightly different cutoff frequencies.
468 Among these sixteen terms, the contribution of $-\partial[\bar{u}]_{>91d}[\bar{\omega}]_{21-90d}/\partial p$, the vertical transport of
469 u-wind with a period longer than 91 days by the MJO-scale vertical motion (red dashed line in Fig.

470 9), accounts for the dominant role for the total large-scale vertical u-momentum transport (black
 471 thick line) over both the IO and WP, although a relatively smaller contribution (about 50%) to the
 472 total large-scale momentum tendency is noted over the WP, particularly in the low-to-mid levels
 473 between 700hPa and 300hPa (Fig. 9b). Vertical u-momentum transport by synoptic time-scale
 474 waves, which has been proposed to play a critical role for the MJO in recent idealized model
 475 studies, however, does not significantly contribute to the total grid-scale momentum as suggested
 476 by the CFSR reanalysis.

477 Since the $-\partial[\bar{u}]_{>91d}[\bar{\omega}]_{21-90d}/\partial p$ term plays such a critical role in the total large-scale
 478 momentum tendency over both the IO and WP, Figure 10 further displays vertical profiles of the
 479 winter mean u-wind ($[\bar{u}]_{d>91}$, (Fig. 10a), and the vertical pressure velocity associated with the
 480 MJO ($[\bar{\omega}]_{21-90d}$, Fig.10b), over the IO (black) and WP (green), respectively. The winter mean
 481 zonal winds over both the IO and WP are characterized by easterly vertical shear (although a much
 482 weaker shear over the WP) with maximum easterlies and westerlies near 150hPa and 850hPa,
 483 respectively. Meanwhile, the vertical velocity associated with the MJO over both regions is
 484 characterized by anomalous upward motion with a maximum near 350hPa, in agreement with the
 485 enhanced MJO convection.

486 In order to further understand the three-layer profiles in large-scale CMT, the term
 487 $-\partial([\bar{u}]_{>91d}[\bar{\omega}]_{21-90d})/\partial p$ is further decomposed into two terms and shown in Fig. 10c,
 488 $-\bar{\omega}]_{21-90d}\partial[\bar{u}]_{>91d}/\partial p$ (green) and $-\bar{u}]_{>91d}\partial[\bar{\omega}]_{21-90d}/\partial p$ (blue). Our results suggest that
 489 both of these terms contribute to the three-layer vertical structure in $-\partial([\bar{u}]_{>91d}[\bar{\omega}]_{21-90d})/\partial p$
 490 (red dashed line as duplicated from Fig. 9a); while the $-\bar{u}]_{>91d}\partial[\bar{\omega}]_{21-90d}/\partial p$ term (blue) is
 491 mainly responsible for the negative grid-scale momentum tendency in the upper-troposphere, the
 492 term $-\bar{\omega}]_{21-90d}\partial[\bar{u}]_{>91d}/\partial p$ (green) is important for the positive anomalies in the lower-to-mid
 493 levels. Both of these terms contribute to relatively weak negative momentum tendency anomalies

494 near the surface. Moreover, the weaker mean easterly vertical wind shear over the WP compared to
495 that over the IO as shown in Fig. 10a, and thus a weaker amplitude in $-\overline{[\bar{\omega}]_{21-90d}}\partial[\bar{u}]_{>91d}/\partial p$
496 (figure not shown), is also consistent with a smaller contribution of $-\partial([\bar{u}]_{>91d}[\bar{\omega}]_{21-90d})/\partial p$ to
497 the total large-scale momentum tendency, particularly in the lower-to-mid troposphere between
498 700-300hPa over the WP as shown in Fig. 9b.

499 **3d. Leading EOF mode of vertical subgrid CMT profile and its modulation by the MJO**

500 In this subsection, vertical profiles of subgrid-scale momentum tendency associated with the
501 MJO are further examined from a different viewpoint. First, we carry out an EOF analysis of
502 vertical momentum tendency profiles over the IO and WP to identify the leading mode of vertical
503 tendency profiles based on the raw 6-hourly subgrid-scale tendency output from the CFSR.
504 Preference of the leading momentum tendency mode relative to a particular MJO phase is then
505 examined by conducting composite analysis of the principal component (PC) coefficients as a
506 function of MJO phase.

507 To be consistent with momentum tendency profiles previously discussed based on a
508 regression approach, two small equatorial regions are selected for the EOF analyses, one over the
509 IO (79°E-81°E, 1°S-1°N) and another over the WP (154°E-155°E, 1°S-1°N). Similar results can be
510 obtained when different locations over the IO or WP are selected for the EOF analysis. Six-hourly
511 vertical profiles (37 levels) of subgrid-scale momentum tendency over these two selected spots
512 during winters from 1998-2010 are obtained based on the raw 50km CFSR output by averaging
513 over these two boxes, and then are subject to the EOF analysis. The first leading mode of vertical
514 subgrid momentum tendency, which is shown in Fig. 11, accounts for 32% and 31% of total
515 variances over the IO and WP, respectively. Of particular interest, a three-layer structure in the
516 vertical momentum tendency profile as previously described, i.e., a positive sign below 850hPa,

517 negative between 850hPa and 300hPa, and positive above 300hPa, is again discerned in the first
518 leading modes over both the IO and WP (Fig. 11a), exhibiting great resemblances to the vertical
519 profiles of regressed subgrid-scale momentum tendency pattern associated with the MJO as shown
520 in Fig. 2. Further composites of coefficients of the first leading PCs over both the IO and WP
521 suggests that occurrence of the first leading subgrid momentum tendency modes is greatly favored
522 during the MJO peak phases (Fig. 11b). For example, the leading vertical momentum tendency
523 mode over the IO is most favored during the MJO phase 3 when the active MJO convection is
524 located over the eastern IO, while the leading subgrid momentum tendency mode over the WP
525 becomes most active during MJO phase 6 when local MJO convection reaches its maximum. The
526 presence of positive composite PCs during the entire MJO cycle over the IO suggests prevalence of
527 the three-layer subgrid CMT profile on the seasonal mean time scale; while over the WP, the CMT
528 tends to be more strongly controlled by the MJO. This intimate association between the preferred
529 vertical 3-layer subgrid-scale momentum tendency profile and MJO peak phases may suggest a
530 two-way interaction between the MJO large-scale circulation and small-scale convection through
531 momentum transport as demonstrated by the idealized model in Majda and Stechmann (2009).

532 Since subgrid-scale momentum tendency from a model parameterization scheme only
533 considers conditions on a local grid point including cumulus mass fluxes and vertical wind profile,
534 representation of impacts from organized MCSs has been a longstanding challenge for current
535 weather and climate models (Tao and Moncrieff 2009; Moncrieff 2010). This model deficiency in
536 resolving the MCSs justifies a mesoscale parameterization approach, for example, by estimating
537 mesoscale momentum transport by using an archetypical dynamical model (Moncrieff 1992). Thus,
538 it could be interesting to examine the mesoscale circulations associated with the first leading
539 subgrid-scale momentum tendency mode based on the CFSR. Figure 12 illustrates regressed
540 patterns of mesoscale circulation by the spatial filtering approach (u' and $-\omega'$; vectors) and vertical

541 flux of zonal momentum $u'w'$ (shaded) against the PC time series of the first EOF mode of subgrid-
542 scale momentum tendency over the IO. Interestingly, associated with the subgrid-scale momentum
543 tendency over the small box over the IO, a well-organized relatively large-scale circulation is
544 evident in the regression pattern with eastward tilting with height. This vertical tilting in circulation
545 and associated vertical u-momentum transport greatly resembles the widely reported vertical
546 structure of the organized convective systems and their impacts on environmental flow (Moncrieff
547 1992; Lemone and Moncrieff 1994; Mapes et al. 2006). As previously discussed, the mesoscale
548 circulation derived based on the CFSR by the spatial filtering approach used in this study likely
549 only marginally captures the observed mesoscale system due to the coarse spatial and temporal
550 resolutions of the reanalysis dataset. Nevertheless, results in this part indicate that, albeit the
551 subgrid-scale CMT is calculated independently on each model grid, to some extent it may still be
552 able to represent collective impacts from large-scale organized convection.

553 **4. Summary and conclusion**

554 While the prominent role of the Madden-Julian Oscillation (MJO) in global climate and
555 weather systems has been fully recognized, skillful simulation and prediction of the MJO still
556 represent great challenges for current climate models, due largely to our insufficient understanding
557 of the multi-scale interactions associated with organized convection. In addition to exchanges of
558 thermodynamical properties between multi-scale convective systems and the MJO, which have
559 been the main focus of previous studies, recent evidence based on limited observations, idealized
560 model studies, as well as full GCM simulations, indicate that momentum transport by organized
561 convection could also play a crucial role in sustaining the MJO circulation. By capitalizing on the
562 new generation high-resolution reanalysis datasets with a long record, particularly on subgrid
563 convective momentum transport (CMT) fields archived from the CFSR reanalysis and explicit

564 momentum transport, we have comprehensively examined the structure of momentum tendency
565 associated with the MJO at different spatial and temporal scales, with particular attention to the
566 vertical transport of u-momentum.

567 A three-layer vertical structure, as previously suggested in the mesoscale momentum tendency
568 pattern associated with the MJO over the WP based on global CRM simulations, is also evident in
569 the subgrid CMT generated by the cumulus parameterization scheme in the CFSR model. In
570 association with enhanced MJO convection over both the IO and WP, within and to the west of the
571 MJO convection, positive, negative, and positive subgrid momentum tendency anomalies are
572 evident in the upper (300-100hPa), middle (800-300hPa), and lower (below 800hPa) troposphere,
573 respectively. A similar three-layer vertical subgrid momentum tendency profile but with an
574 opposite sign is observed to the east of the MJO convection. This subgrid CMT vertical structure,
575 on the one hand, tends to damp the large-scale MJO circulation in the free atmosphere above
576 800hPa, but enhances MJO winds in a shallow near-surface layer below 800hPa. On the other hand,
577 a tendency in generating a secondary circulation by this three-layer subgrid profile near the MJO
578 convection center could retard the eastward propagation of the MJO in the free atmosphere, while
579 promoting the eastward propagation near the surface. As a result, the total momentum tendency
580 could be partially responsible for the backward tilt with height in the observed MJO structure.

581 Further analyses based on 50km CFSR reanalysis illustrate that u-momentum transport
582 associated with the MJO by grid-scale circulation exhibits a similar three-layer vertical structure
583 and comparable amplitude as the subgrid CMT, but with an opposite sign. Total grid-scale CMT is
584 further decomposed into a mesoscale and a remaining large-scale component following a spatial
585 scale separation approach with a cut-off scale of 5-deg radius for the mesoscale system. As
586 expected, the mesoscale CMT has a very weak amplitude due to the 50km horizontal resolution of
587 the CFSR data, and the total grid-scale momentum tendency is predominantly contributed by the

588 large-scale circulation transport. It is noteworthy that, in spite of its weak amplitude, the vertical
589 structure in mesoscale CMT associated with the MJO greatly resembles the subgrid CMT, and in
590 agreement with that by the 7-km CRM simulations in Miyakawa et al. (2012). This suggests that
591 although CMT by mesoscale systems cannot be fully resolved in the CFSR data at a 50km
592 resolution, the subgrid CMT from the cumulus parameterization scheme may at least partly
593 represent mesoscale CMT impacts as depicted in the previous CRM study. This notion is further
594 supported by the well-organized vertically tilted mesoscale circulation obtained by regressing
595 mesoscale filtered momentum tendency fields against an index corresponding to the leading EOF
596 mode of the subgrid momentum tendency as shown in Section 3d.

597 It is further suggested that vertical u-momentum transport by large-scale circulation is mainly
598 ascribed to transport of seasonal mean u-wind by the MJO time-scale vertical motion. Vertical u-
599 momentum transport by synoptic time-scale waves, which has been proposed to play a critical role
600 for the MJO in recent idealized model studies, however, does not significantly contribute to the
601 total grid-scale CMT based on the analyses in this study based on the CFSR reanalysis.

602 One of the main findings from this study is that the subgrid CMT by the model
603 parameterization (which could include mesoscale CMT in reality) could play an important role for
604 the u-momentum budget associated with the MJO by largely offsetting the vertical grid-scale
605 momentum transport induced by the MJO circulation itself. Therefore, if CMT impacts by small
606 scale convective systems are not properly represented in a GCM, the grid-scale momentum
607 transport needs to be balanced by other terms; it thus could lead to model biases in simulating the
608 MJO circulation. Cancellation between the subgrid and grid-scale momentum tendencies was also
609 noted in CRM simulations by Mapes and Wu (2001) and in global weather forecasts by the
610 ECMWF model (MK97, their Fig. 8). This is likely due to the fact that CMT processes are strong
611 functions of the environmental vertical shear. For subgrid momentum tendency, this involves

612 compensating downwelling associated with the convective updraft (see 1st term on the r.h.s. of Eq.
613 1), while for the grid-scale tendency, the transport is accomplished by the tilted organized
614 circulations.

615 One caveat of this study is that subgrid CMT output from the CFSR reanalysis is sensitive to
616 the parameterization scheme. Also, due to limitation in the horizontal resolution, the CMT impact
617 on the MJO due to mesoscale systems cannot be well resolved in the CFSR model. In order to
618 provide an independent validation of the results derived from CFSR reanalyses, vertical CMT
619 profiles associated with the MJO by subgrid, mesoscale, as well as large-scale processes are also
620 analyzed by using the EC-YOTC reanalysis during the period of two years. Largely similar results
621 in CMT structure by the different spatial / time scales as shown based on the CFSR reanalysis are
622 also evident in the analyses based on the EC-YOTC dataset. This further lends confidence to the
623 findings derived in this study based on the CFSR reanalysis.

624 Our results from the reanalyses, already noted as consistent with Miyakawa et al. (2012), are
625 also consistent with the MK97 study of large-scale convective organization in the context of MJO
626 observed during TOGA COARE and simulated by the ECMWF model on a 80km grid.
627 Specifically, they found that the subgrid momentum tendency was dominated by, and had an
628 opposite sign from, the meso-to-large scale momentum tendency associated with super clusters.
629 The momentum tendency was approximated using the Moncrieff (1992) archetypal dynamical
630 model of organized convection in sheared environments which represents upscale transport relevant
631 to the organized deep convection phase of the MJO and the associated westerly wind bursts.

632 While results in this study as well as other previous observational and modeling studies
633 suggest that the subgrid CMT could play an important role for the observed MJO, it may not be the
634 primary factor responsible for realistic representation of the MJO in a GCM. For example, even
635 without including subgrid CMT impacts on the large-scale flow, a super-parameterized GCM, in

636 which a 2D CRM is embedded within each grid box of the host model to replace the conventional
637 cumulus parameterizations (Randall et al. 2003), can still largely capture the most important
638 features of the observed MJO (e.g., Benedict and Randall 2009; Pritchard and Bretherton 2014).
639 However, deficiencies were also noted in these super-parametrized GCM experiments, e.g., an
640 overestimate of the intraseasonal convective activity over the WP (Benedict and Randall 2009),
641 which are likely due to unrealistic boundary layer interactions, a lack of weakening of the simulated
642 disturbance over the Maritime Continent, and mean state differences (Benedict and Randall 2009).
643 Additionally, based on a recent global MJO model inter-comparison project (Jiang et al. 2015), the
644 two versions of super-parameterized GCMs, one with atmosphere-only run, and another with
645 atmosphere-ocean coupling, actually were not the top models in simulating the MJO among the
646 total 27 models participated in this project. Both of the two super-parameterized model experiments
647 exhibit large room for improvement in simulating the MJO. Therefore, missing processes in
648 describing the subgrid CMT feedbacks in these super-parameterized GCM experiments could be
649 partly responsible for the above model deficiencies.

650 Future studies warrant further investigations of the relative roles of different spatial- and
651 temporal- scale systems for the total momentum transport associated with the MJO based on CRM
652 simulations with a long record. A particular advantage of the CRM is the more complete resolution
653 of mesoscale convective systems. Definitive observations are also needed to quantify important
654 scale dependent aspects and to evaluate CRM results. The most recent observations available from
655 the DYNAMO (Dynamics of the Madden-Julian Oscillation; Yoneyama et al. 2013) field campaign
656 may provide new insights into the role of the convective momentum transport associated with the
657 MJO.

658 **Acknowledgment**

659 We thank anonymous reviewers for their critical comments on an earlier version of this paper. This
660 work has greatly benefited from stimulating discussions with Drs. A. Majda, T. Miyakawa, B.
661 Mapes, M. Zhao, and G. Zhang, and helpful comments from Drs. J. Stachnik, J. Han, and T. Kubar.
662 We acknowledge support by the NSF Climate and Large-Scale Dynamics Program under Awards
663 AGS-1228302 and AGS-1221013, and NOAA MAPP Program under Award NA12OAR4310075.
664 Part of this research was carried out at the Jet Propulsion Laboratory, California Institute of
665 Technology, under a contract with the National Aeronautics and Space Administration. NCAR is
666 sponsored by the National Science Foundation.

667

668 **References**

669

- 670 Ajayamohan, R. S., B. Khouider, and A. J. Majda, 2013: Realistic initiation and dynamics of the
671 Madden-Julian Oscillation in a coarse resolution aquaplanet GCM. *Geophys. Res. Lett.*, **40**,
672 10.1002/2013GL058187, 6252-6257.
- 673 Arakawa, A. and W. H. Schubert, 1974: Interaction of a Cumulus Cloud Ensemble with Large-
674 Scale Environment .1. *J. Atmos. Sci.*, **31**, 674-701.
- 675 Benedict, J. J. and D. A. Randall, 2009: Structure of the Madden-Julian Oscillation in the
676 Superparameterized CAM. *J. Atmos. Sci.*, **66**, 3277-3296.
- 677 Carr, M. T. and C. S. Bretherton, 2001: Convective Momentum Transport over the Tropical Pacific:
678 Budget Estimates. *J. Atmos. Sci.*, **58**, doi:10.1175/1520-0469, 1673-1693.
- 679 Chen, S. S., R. A. Houze, and B. E. Mapes, 1996: Multiscale variability of deep convection in
680 relation to large-scale circulation in TOGA COARE. *J. Atmos. Sci.*, **53**, 1380-1409.
- 681 Del Genio, A. D., Y. Chen, D. Kim, and M.-S. Yao, 2012: The MJO Transition from Shallow to
682 Deep Convection in CloudSat/CALIPSO Data and GISS GCM Simulations. *J. Clim.*, **25**,
683 10.1175/JCLI-D-11-00384.1, 3755-3770.
- 684 Deng, L. and X. Wu, 2010: Effects of Convective Processes on GCM Simulations of the Madden-
685 Julian Oscillation. *J. Clim.*, **23**, 10.1175/2009jcli3114.1, 352-377.
- 686 Duchon, C. E., 1979: Lanczos Filtering in One and Two Dimensions. *J. Appl. Meteorol.*, **18**, 1016-
687 1022.
- 688 Han, Y. and B. Khouider, 2010: Convectively Coupled Waves in a Sheared Environment. *J. Atmos.*
689 *Sci.*, **67**, doi:10.1175/2010JAS3335.1, 2913-2942.
- 690 Houze, R. A., 1973: Climatological Study of Vertical Transports by Cumulus-Scale Convection. *J.*
691 *Atmos. Sci.*, **30**, 1112-1123.
- 692 ———, 2004: Mesoscale convective systems. *Rev. Geophys.*, **42**, doi: 10.1029/2004RG000150.
- 693 Houze, R. A., S. S. Chen, D. E. Kingsmill, Y. Serra, and S. E. Yuter, 2000: Convection over the
694 Pacific warm pool in relation to the atmospheric Kelvin-Rossby wave. *J. Atmos. Sci.*, **57**,
695 3058-3089.

- 696 Huffman, G. J., R. F. Adler, B. Rudolf, U. Schneider, and P. R. Keehn, 1995: Global Precipitation
697 Estimates Based on a Technique for Combining Satellite-Based Estimates, Rain-Gauge
698 Analysis, and Nwp Model Precipitation Information. *J. Clim.*, **8**, 1284-1295.
- 699 Hung, M.-P., J.-L. Lin, W. Wang, D. Kim, T. Shinoda, and S. J. Weaver, 2013: MJO and
700 Convectively Coupled Equatorial Waves Simulated by CMIP5 Climate Models. *J. Clim.*,
701 **26**, 10.1175/JCLI-D-12-00541.1, 6185-6214.
- 702 Jiang, X., D. Waliser, J.-L. Li, and C. Woods, 2011: Vertical cloud structures of the boreal summer
703 intraseasonal variability based on CloudSat observations and ERA-interim reanalysis.
704 *Climate Dyn.*, **36**, 10.1007/s00382-010-0853-8, 2219-2232.
- 705 Jiang, X., et al., 2015: Vertical structure and physical processes of the Madden-Julian Oscillation:
706 Exploring key model physics in climate simulations. *Journal of Geophysical Research -*
707 *Atmosphere*, in press.
- 708 Johnson, R. H., T. M. Rickenbach, S. A. Rutledge, P. E. Ciesielski, and W. H. Schubert, 1999:
709 Trimodal Characteristics of Tropical Convection. *J. Clim.*, **12**, 2397-2418.
- 710 Khouider, B. and A. J. Majda, 2006a: Model multi-cloud parameterizations for convectively
711 coupled waves: Detailed nonlinear wave evolution. *Dynamics of Atmospheres and Oceans*,
712 **42**, 59-80.
- 713 ———, 2006b: A Simple Multicloud Parameterization for Convectively Coupled Tropical Waves.
714 Part I: Linear Analysis. *J. Atmos. Sci.*, **63**, 1308-1323.
- 715 ———, 2007: A Simple Multicloud Parameterization for Convectively Coupled Tropical Waves. Part
716 II: Nonlinear Simulations. *J. Atmos. Sci.*, **64**, 381-400.
- 717 Khouider, B. and A. J. Majda, 2008a: Multicloud models for organized tropical convection:
718 Enhanced congestus heating. *J. Atmos. Sci.*, **65**, Doi 10.1175/2007jas2408.1, 895-914.
- 719 Khouider, B. and A. J. Majda, 2008b: Equatorial Convectively Coupled Waves in a Simple
720 Multicloud Model. *J. Atmos. Sci.*, **65**, 3376-3397.
- 721 Khouider, B., Y. Han, and J. A. Biello, 2012a: Convective Momentum Transport in a Simple
722 Multicloud Model for Organized Convection. *J. Atmos. Sci.*, **69**, Doi 10.1175/Jas-D-11-
723 042.1, 281-302.
- 724 Khouider, B., A. St-Cyr, A. J. Majda, and J. Tribbia, 2011: The MJO and Convectively Coupled
725 Waves in a Coarse-Resolution GCM with a Simple Multicloud Parameterization. *J. Atmos.*
726 *Sci.*, **68**, 10.1175/2010jas3443.1, 240-264.
- 727 Khouider, B., Y. Han, A. J. Majda, and S. N. Stechmann, 2012b: Multiscale Waves in an MJO
728 Background and Convective Momentum Transport Feedback. *J. Atmos. Sci.*, **69**,
729 10.1175/JAS-D-11-0152.1, 915-933.
- 730 Kikuchi, K. and Y. N. Takayabu, 2004: The development of organized convection associated with
731 the MJO during TOGA COARE IOP: Trimodal characteristics. *Geophys. Res. Lett.*, **31**.
- 732 Kikuchi, K. and B. Wang, 2010: Spatiotemporal Wavelet Transform and the Multiscale Behavior of
733 the Madden-Julian Oscillation*. *J. Clim.*, **23**, 10.1175/2010jcli2693.1, 3814-3834.
- 734 Kiladis, G. N., M. C. Wheeler, P. T. Haertel, K. H. Straub, and P. E. Roundy, 2009: Convectively
735 Coupled Equatorial Waves. *Rev. Geophys.*, **47**, RG2003, DOI:10.1029/2008RG000266
- 736 Kim, D., J. S. Kug, I. S. Kang, F. F. Jin, and A. T. Wittenberg, 2008: Tropical Pacific impacts of
737 convective momentum transport in the SNU coupled GCM. *Climate Dyn.*, **31**, DOI
738 10.1007/s00382-007-0348-4, 213-226.
- 739 Kim, D., et al., 2009: Application of MJO Simulation Diagnostics to Climate Models. *J. Clim.*, **22**,
740 Doi 10.1175/2009jcli3063.1, 6413-6436.
- 741 Kiranmayi, L. and E. D. Maloney, 2011: Intraseasonal moist static energy budget in reanalysis data.
742 *Journal of Geophysical Research: Atmospheres*, **116**, 10.1029/2011JD016031, D21117.

- 743 Lau, W. K.-M. and D. E. Waliser, 2012: *Intraseasonal Variability in the Atmosphere-Ocean*
744 *Climate System*. Second ed. Springer, 613p, Heidelberg, Germany.
- 745 Lemone, M. A. and M. W. Moncrieff, 1994: Momentum and Mass-Transport by Convective Bands
746 - Comparisons of Highly Idealized Dynamical Models to Observations. *J. Atmos. Sci.*, **51**,
747 281-305.
- 748 Lin, J.-L., et al., 2006: Tropical Intraseasonal Variability in 14 IPCC AR4 Climate Models. Part I:
749 Convective Signals. *J. Clim.*, **19**, 2665-2690.
- 750 Lin, J. L., M. H. Zhang, and B. Mapes, 2005: Zonal momentum budget of the Madden-Julian
751 oscillation: The source and strength of equivalent linear damping. *J. Atmos. Sci.*, **62**, 2172-
752 2188.
- 753 Lin, J. L., B. E. Mapes, and W. Q. Han, 2008: What are the sources of mechanical damping in
754 Matsuno-Gill-type models? *J. Clim.*, **21**, Doi 10.1175/2007jcli1546.1, 165-179.
- 755 Lin, X. and R. H. Johnson, 1996: Heating, moistening, and rainfall over the western Pacific warm
756 pool during TOGA COARE. *J. Atmos. Sci.*, **53**, 3367-3383.
- 757 Madden, R. A. and P. R. Julian, 1971: Detection of a 40-50 Day Oscillation in Zonal Wind in
758 Tropical Pacific. *J. Atmos. Sci.*, **28**, 702-&.
- 759 ———, 1994: Observations of the 40-50-Day Tropical Oscillation: A Review. *Mon. Weather Rev.*,
760 **122**, 814-837.
- 761 Majda, A. J., 2007: New Multiscale Models and Self-Similarity in Tropical Convection. *J. Atmos.*
762 *Sci.*, **64**, 1393-1404.
- 763 Majda, A. J. and J. A. Biello, 2004: A multiscale model for tropical intraseasonal oscillations. *Proc.*
764 *Natl. Acad. Sci.*, **101**, 4736-4741.
- 765 Majda, A. J. and S. N. Stechmann, 2008: Stochastic models for convective momentum transport.
766 *Proceedings of the National Academy of Sciences*, **105**, 10.1073/pnas.0806838105, 17614-
767 17619.
- 768 ———, 2009: A Simple Dynamical Model with Features of Convective Momentum Transport. *J.*
769 *Atmos. Sci.*, **66**, 373-392.
- 770 Majda, A. J. and S. N. Stechmann, 2011: Multi-scale theories for the MJO. *Intraseasonal*
771 *Variability in the Atmosphere-Ocean Climate System*, Second ed. W. K. M. Lau and D. E.
772 Waliser, Eds., Springer, Heidelberg, Germany, In Press.
- 773 ———, 2014: Models for Multiscale Interactions, II: Madden-Julian Oscillation, Moisture, and
774 Convective Momentum Transport. *Multiscale Convection-Coupled Systems in the Tropics:*
775 *A Tribute to Michio Yanai*. American Meteorological Society Monographs. Tung W-W,
776 Fovell R, Matsuno T (editors).
- 777 Mapes, B., S. Tulich, J. Lin, and P. Zuidema, 2006: The mesoscale convection life cycle: Building
778 block or prototype for large-scale tropical waves? *Dynamics of Atmospheres and Oceans*,
779 **42**, Doi 10.1016/J.Dynatmoce.2006.03.003, 3-29.
- 780 Mapes, B. E. and X. Wu, 2001: Convective Eddy Momentum Tendencies in Long Cloud-Resolving
781 Model Simulations. *J. Atmos. Sci.*, **58**, doi:10.1175/1520-0469, 517-526.
- 782 Mapes, B. E. and J. T. Bacmeister, 2012: Diagnosis of Tropical Biases and the MJO from Patterns
783 in the MERRA Analysis Tendency Fields. *J. Clim.*, **25**, 10.1175/jcli-d-11-00424.1, 6202-
784 6214.
- 785 Miura, H., M. Satoh, T. Nasuno, A. T. Noda, and K. Oouchi, 2007: A Madden-Julian Oscillation
786 event realistically simulated by a global cloud-resolving model. *Science*, **318**, Doi
787 10.1126/Science.1148443, 1763-1765.
- 788 Miyakawa, T., Y. N. Takayabu, T. Nasuno, H. Miura, M. Satoh, and M. W. Moncrieff, 2012:
789 Convective Momentum Transport by Rainbands within a Madden-Julian Oscillation in a

790 Global Nonhydrostatic Model with Explicit Deep Convective Processes. Part I:
 791 Methodology and General Results. *J. Atmos. Sci.*, **69**, 10.1175/jas-d-11-024.1, 1317-1338.

792 Moncrieff, M. W., 1992: Organized Convective Systems - Archetypal Dynamic-Models, Mass and
 793 Momentum Flux Theory, and Parametrization. *Quart. J. Roy. Meteor. Soc.*, **118**, 819-850.

794 ———, 2010: The multiscale organization of convection at the intersection of weather and climate.
 795 *Why does Climate Vary? AGU Geophysical Monograph Series, 189*, D. Sun and F. Bryan,
 796 Eds.3-26.

797 Moncrieff, M. W. and E. Klinker, 1997: Organized convective systems in the tropical western
 798 Pacific as a process in general circulation models: A TOGA COARE case-study. *Quart. J.*
 799 *Roy. Meteor. Soc.*, **123**, 10.1002/qj.49712354002, 805-827.

800 Moncrieff, M. W., D. E. Waliser, M. J. Miller, M. A. Shapiro, G. R. Asrar, and J. Caughey, 2012:
 801 Multiscale Convective Organization and the YOTC Virtual Global Field Campaign. *Bull.*
 802 *Am. Meteorol. Soc.*, **93**, 10.1175/bams-d-11-00233.1, 1171-1187.

803 Moorthi, S., H.-L. Pan, and P. Caplan, 2001: Changes to the 2001 NCEP operational MRF/AVN
 804 global analysis/forecast system. NWS Tech. Procedures Bull. 484, 14 pp.

805 Nakazawa, T., 1988: Tropical Super Clusters within Intraseasonal Variations over the Western
 806 Pacific. *J. Meteorol. Soc. Japan*, **66**, 823-839.

807 Neelin, J. D. and I. M. Held, 1987: Modeling Tropical Convergence Based on the Moist Static
 808 Energy Budget. *Mon. Weather Rev.*, **115**, 3-12.

809 Pan, H. and W. Wu, 1995: Implementing a mass flux convective parameterization package for the
 810 NMC medium range forecast model. NMC Office Note 409, 40 pp.

811 Pritchard, M. S. and C. S. Bretherton, 2014: Causal Evidence that Rotational Moisture Advection is
 812 Critical to the Superparameterized Madden–Julian Oscillation. *J. Atmos. Sci.*, **71**,
 813 10.1175/JAS-D-13-0119.1, 800-815.

814 Randall, D., M. Khairoutdinov, A. Arakawa, and W. Grabowski, 2003: Breaking the Cloud
 815 Parameterization Deadlock. *Bull. Am. Meteorol. Soc.*, **84**, 10.1175/BAMS-84-11-1547,
 816 1547-1564.

817 Rauniyar, S. P. and K. J. E. Walsh, 2011: Scale Interaction of the Diurnal Cycle of Rainfall over the
 818 Maritime Continent and Australia: Influence of the MJO. *J. Clim.*, **24**,
 819 doi:10.1175/2010JCLI3673.1, 325-348.

820 Raymond, D. J., S. Sessions, A. Sobel, and Z. Fuchs, 2009: The Mechanics of Gross Moist
 821 Stability. *Journal of Advances in Modeling Earth Systems*, **1**, 10.3894/james.2009.1.9, 20
 822 pp.

823 Richter, J. H. and P. J. Rasch, 2008: Effects of convective momentum transport on the atmospheric
 824 circulation in the community atmosphere model, version 3. *J. Clim.*, **21**, Doi
 825 10.1175/2007jcli1789.1, 1487-1499.

826 Roundy, P. E., 2008: Analysis of convectively coupled Kelvin waves in the Indian ocean MJO. *J.*
 827 *Atmos. Sci.*, **65**, Doi 10.1175/2007jas2345.1, 1342-1359.

828 Saha, S., et al., 2010: The NCEP Climate Forecast System Reanalysis. *Bull. Am. Meteorol. Soc.*, **0**,
 829 doi:10.1175/2010BAMS3001.1.

830 Satoh, M., T. Matsuno, H. Tomita, H. Miura, T. Nasuno, and S. Iga, 2008: Nonhydrostatic
 831 icosahedral atmospheric model (NICAM) for global cloud resolving simulations. *Journal of*
 832 *Computational Physics*, **227**, Doi 10.1016/J.jcp.2007.02.006, 3486-3514.

833 Schumacher, C. and R. A. Houze, 2003: Stratiform rain in the tropics as seen by the TRMM
 834 precipitation radar. *J. Clim.*, **16**, 1739-1756.

835 Shapiro, L. J. and D. E. Stevens, 1980: Parameterization of Convective Effects on the Momentum
 836 and Vorticity Budgets of Synoptic-Scale Atlantic Tropical Waves. *Mon. Weather Rev.*, **108**,
 837 1816-1826.

- 838 Sherwood, S. C., 1999: Convective precursors and predictability in the tropical western Pacific.
839 *Mon. Weather Rev.*, **127**, Doi 10.1175/1520-0493(1999)127<2977:Cpapit>2.0.Co;2, 2977-
840 2991.
- 841 Slingo, J. M., et al., 1996: Intraseasonal oscillations in 15 atmospheric general circulation models:
842 Results from an AMIP diagnostic subproject. *Climate Dyn.*, **12**, 325-357.
- 843 Song, X., X. Wu, G. J. Zhang, and R. W. Arritt, 2008: Understanding the Effects of Convective
844 Momentum Transport on Climate Simulations: The Role of Convective Heating. *J. Clim.*,
845 **21**, doi:10.1175/2008JCLI2187.1, 5034-5047.
- 846 Takaya, K. and H. Nakamura, 2001: A Formulation of a Phase-Independent Wave-Activity Flux for
847 Stationary and Migratory Quasigeostrophic Eddies on a Zonally Varying Basic Flow. *J.*
848 *Atmos. Sci.*, **58**, 608-627.
- 849 Takayabu, Y. N., 1994: Large-Scale Cloud Disturbances Associated with Equatorial Waves .1.
850 Spectral Features of the Cloud Disturbances. *J. Meteorol. Soc. Japan*, **72**, 433-449.
- 851 Takayabu, Y. N. and M. Murakami, 1991: The Structure of Super Cloud Clusters Observed in 1-20
852 June 1986 and their Relationship to Easterly Waves. *Journal of the Meteorological Society*
853 *of Japan. Ser. II*, **69**, 105-125.
- 854 Takayabu, Y. N., K. M. Lau, and C. H. Sui, 1996: Observation of a Quasi-2-Day Wave during
855 TOGA COARE. *Mon. Weather Rev.*, **124**, 10.1175/1520-
856 0493(1996)124<1892:OOAQDW>2.0.CO;2, 1892-1913.
- 857 Tao, W. K. and M. W. Moncrieff, 2009: MULTISCALE CLOUD SYSTEM MODELING. *Rev.*
858 *Geophys.*, **47**, 10.1029/2008rg000276.
- 859 Tung, W. W. and M. Yanai, 2002a: Convective momentum transport observed during the TOGA
860 COARE IOP. Part II: Case studies. *J. Atmos. Sci.*, **59**, 2535-2549.
- 861 ———, 2002b: Convective momentum transport observed during the TOGA COARE IOP. Part I:
862 General features. *J. Atmos. Sci.*, **59**, 1857-1871.
- 863 Waliser, D. E., et al., 2012: The “Year” of Tropical Convection (May 2008–April 2010): Climate
864 Variability and Weather Highlights. *Bull. Am. Meteorol. Soc.*, **93**,
865 10.1175/2011BAMS3095.1, 1189-1218.
- 866 Wang, B. and T. M. Li, 1994: Convective Interaction with Boundary-Layer Dynamics in the
867 Development of a Tropical Intraseasonal System. *J. Atmos. Sci.*, **51**, 1386-1400.
- 868 Wang, B. and F. Liu, 2011: A Model for Scale Interaction in the Madden–Julian Oscillation. *J.*
869 *Atmos. Sci.*, **68**, 10.1175/2011jas3660.1, 2524-2536.
- 870 Webster, P. J. and R. Lukas, 1992: Toga Coare - the Coupled Ocean Atmosphere Response
871 Experiment. *Bull. Am. Meteorol. Soc.*, **73**, 1377-1416.
- 872 Wheeler, M. C. and H. H. Hendon, 2004: An All-Season Real-Time Multivariate MJO Index:
873 Development of an Index for Monitoring and Prediction. *Mon. Weather Rev.*, **132**, 1917-
874 1932.
- 875 Wu, X., L. Deng, X. Song, G. Vettoretti, W. R. Peltier, and G. J. Zhang, 2007: Impact of a modified
876 convective scheme on the Madden-Julian Oscillation and El Niño–Southern Oscillation in a
877 coupled climate model. *Geophys. Res. Lett.*, **34**, 10.1029/2007GL030637, L16823.
- 878 Yang, G. Y. and J. Slingo, 2001: The diurnal cycle in the Tropics. *Mon. Weather Rev.*, **129**, 784-
879 801.
- 880 Yoneyama, K., C. Zhang, and C. N. Long, 2013: Tracking Pulses of the Madden–Julian Oscillation.
881 *Bull. Am. Meteorol. Soc.*, **94**, 10.1175/BAMS-D-12-00157.1, 1871-1891.
- 882 Yuan, J. and R. A. Houze, 2010: Global Variability of Mesoscale Convective System Anvil
883 Structure from A-Train Satellite Data. *J. Clim.*, **23**, 10.1175/2010jcli3671.1, 5864-5888.

- 884 Zhang, C., J. Gottschalck, E. D. Maloney, M. W. Moncrieff, F. Vitart, D. E. Waliser, B. Wang, and
885 M. C. Wheeler, 2013: Cracking the MJO nut. *Geophys. Res. Lett.*, **40**, 10.1002/grl.50244,
886 1223-1230.
- 887 Zhang, C. D., 2005: Madden-Julian oscillation. *Rev. Geophys.*, **43**, RG2003, DOI:
888 10.1029/2004RG000158, 36.
- 889 Zhou, L., R. B. Neale, M. Jochum, and R. Murtugudde, 2012: Improved Madden-Julian
890 Oscillations with Improved Physics: The Impact of Modified Convection Parameterizations.
891 *J. Clim.*, **25**, Doi 10.1175/2011jcli4059.1, 1116-1136.

892 **Figure Captions**

893 Figure 1. MJO phase-longitude diagrams of composite precipitation anomalies (mm day^{-1}) based on
894 (a) TRMM and (b) CFSR. MJO phases are derived from the MJO life-cycle composite based
895 on the Wheeler-Hendon MJO index. Rainfall anomalies are averaged between 5°S - 5°N in
896 both plots.

897 Figure 2. Longitude-height cross-section of subgrid-scale momentum tendency regressed onto the
898 IO (a) and WP (b) MJO indices, respectively. Shaded color shows the regressed subgrid
899 momentum tendency ($\text{m s}^{-1} \text{ day}^{-1}$), and green lines depict the 20-90-day band-pass filtered
900 precipitation (mm day^{-1} ; right axes). Vectors denote the 20-90-day band-pass filtered wind
901 vectors whose horizontal component is the zonal wind (m s^{-1}), and the vertical component is
902 the pressure velocity (Pa s^{-1} , multiplied by a factor of -100). All values are averaged between
903 5°S - 5°N .

904 Figure 3. Spatial patterns of regressed subgrid-scale momentum tendency (shaded, $\text{m s}^{-1} \text{ day}^{-1}$) at
905 200hPa (top), 500hPa (middle), and 900hPa (bottom), and 20-90-day filtered precipitation
906 anomalies (green contour, mm day^{-1}) onto the IO (left) and WP (right) MJO indices.

907 Figure 4 (a) Same as Fig. 2a, but for zonal divergence of subgrid momentum tendency (shaded; 10^{-6}
908 $\text{s}^{-1} \text{ day}^{-1}$); (b-d): Same as Fig. 3a-c, but with zonal divergence of subgrid CMT for the shaded
909 contours ($10^{-6} \text{ s}^{-1} \text{ day}^{-1}$).

910 Figure 5 Standard deviation of the mesoscale rain derived by the spatial-scale separation (mm day^{-1})
911 based on the CFSR for 12 winters (NDJFMA).

912 Figure 6 Longitude-height diagrams of 5°S - 5°N averaged grid-scale u-momentum tendency (m s^{-1}
913 day^{-1}) by: (a), (d) total vertical momentum transport, $-\partial(u\omega)/\partial p$, (b), (e) meso-scale CMT,
914 $-\partial(u'\omega')/\partial p$, and (c), (f) large-scale momentum transport, $-\partial(\bar{u}\bar{\omega})/\partial p$ regressed onto MJO
915 indices over the IO (a-c), and WP(d-f). For the sake of comparison, $-\partial(u'\omega')/\partial p$ is
916 multiplied by a factor of 4. The green lines and vectors are the same as in Fig. 2, denoting
917 corresponding regressed rainfall anomalies (mm day^{-1}) and circulations.

918 Figure 7 Vertical profiles of u-momentum tendencies ($\text{m s}^{-1} \text{ day}^{-1}$) by zonal (black), meridional
919 (blue), and vertical (red) transports by: (a) total grid-scale; (b) large-scale, and (c) mesoscale
920 circulations, respectively, based on the regression onto the IO MJO index. Note the different
921 scale in the x-axis of (c). All variables are averaged over the regions of $75^{\circ}\text{E}-85^{\circ}\text{E}$, $5^{\circ}\text{S}-5^{\circ}\text{N}$.

922 Figure 8 Longitude-height plots of momentum tendency based on the EC-YOTC analysis (shaded,
923 units: $\text{m s}^{-1} \text{ day}^{-1}$) by: (a) subgrid-scale, (b) mesoscale, (c) large-scale, and (d) total grid scale
924 vertical transports derived by regressions onto the IO MJO index. The mesoscale momentum
925 tendency in (b) is multiplied by a factor of 4. The green lines and vectors are the same as in
926 Fig. 2 but based on the EC-YOTC analysis. All values are averaged between $5^{\circ}\text{S}-5^{\circ}\text{N}$.

927 Figure 9 Vertical profiles of large-scale u-momentum tendency ($\text{m s}^{-1} \text{ day}^{-1}$) due to vertical
928 transport by circulations on various time scales based on regressions against the IO (a) and
929 WP (b) MJO indices. Values are averaged over $75^{\circ}\text{E}-85^{\circ}\text{E}$, $5^{\circ}\text{S}-5^{\circ}\text{N}$ in (a) and $150^{\circ}\text{E}-160^{\circ}\text{E}$,
930 $5^{\circ}\text{S}-5^{\circ}\text{N}$ in (b). The black solid lines represent total large-scale vertical transports.

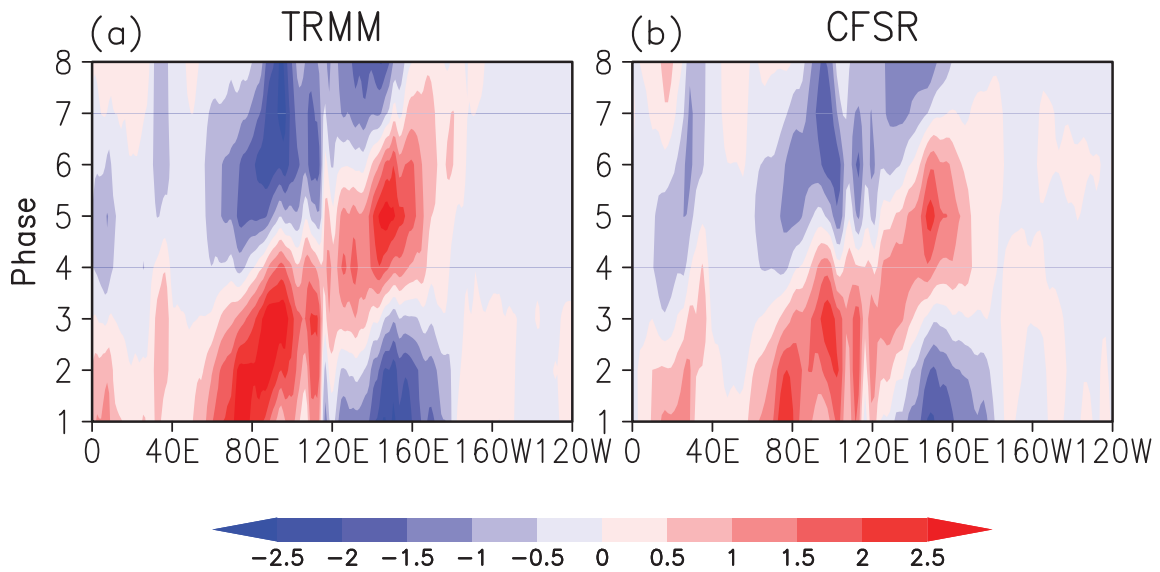
931 Figure 10 Vertical profiles of (a) winter mean zonal wind (m s^{-1}), (b) 21-90 day band-pass filtered
932 vertical pressure velocity (Pa s^{-1}) regressed against the MJO index for the IO ($75^{\circ}\text{E}-85^{\circ}\text{E}$,
933 $5^{\circ}\text{S}-5^{\circ}\text{N}$; black) and the WP ($150^{\circ}\text{E}-160^{\circ}\text{E}$, $5^{\circ}\text{S}-5^{\circ}\text{N}$; green); (c): The
934 $-\partial([\bar{u}]_{>91d}[\bar{\omega}]_{21-90d})/\partial p$ term over the IO (red dashed, duplicated from Fig. 9a; units: m s^{-1}
935 day^{-1}), and its decomposition into $-[\bar{\omega}]_{21-90d}\partial[\bar{u}]_{>91d}/\partial p$ (green) and
936 $-\bar{u}]_{>91d}\partial[\bar{\omega}]_{21-90d}/\partial p$ (blue).

937 Figure 11 (a) Vertical profiles of the first leading EOF mode of subgrid momentum tendency over
938 the IO (black) and WP (green); (b) Corresponding composite PC coefficients as a function of
939 the RMM MJO phases.

940 Figure 12 Pressure-longitude profiles of the subgrid-scale CMT ($-u'\omega'$; shaded) and circulation
941 (vectors; horizontal for zonal winds u' with units of m s^{-1} and vertical for the pressure velocity
942 ω' with units of Pa s^{-1} and multiplied by a factor of -10 for display) derived by regression onto
943 the PC time series of the first leading EOF of the subgrid momentum tendency over the IO.

944

945



946

947 Figure 1. MJO phase-longitude diagrams of composite precipitation anomalies (mm day^{-1}) based on
948 (a) TRMM and (b) CFSR. MJO phases are derived from the MJO life-cycle composite based
949 on the Wheeler-Hendon MJO index. Rainfall anomalies are averaged between 5°S - 5°N in
950 both plots.

951

952

953

954

955

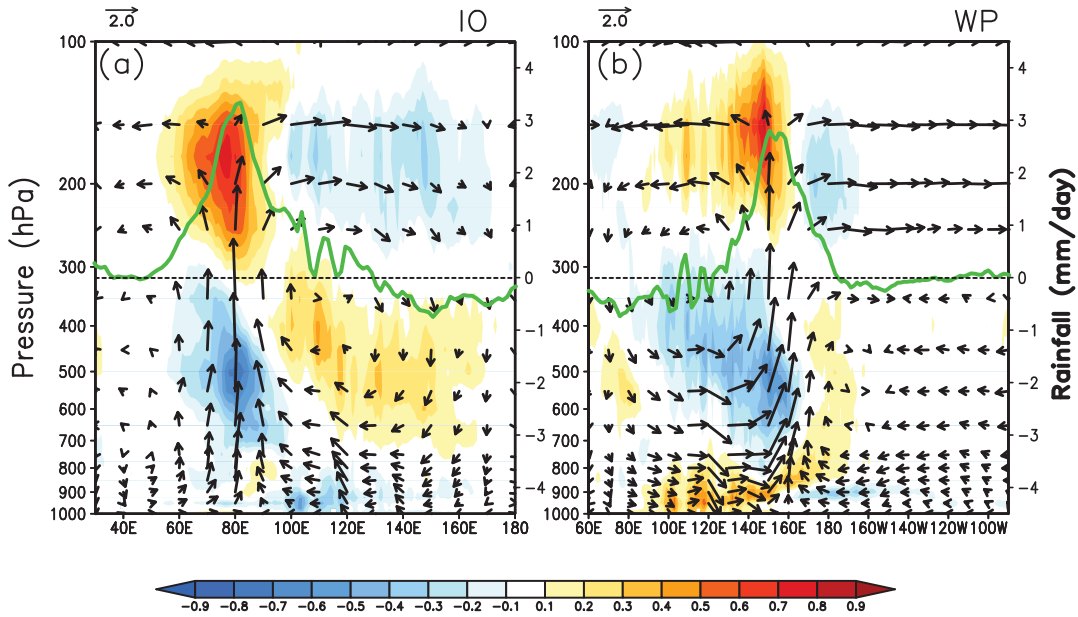
956

957

958

959

960



961

962 Figure 2. Longitude-height cross-sections of subgrid-scale momentum tendency regressed onto the
963 IO (a) and WP (b) MJO indices, respectively. Shaded color shows the regressed subgrid
964 momentum tendency ($\text{m s}^{-1} \text{ day}^{-1}$), and green lines depict the 20-90-day band-pass filtered
965 precipitation (mm day^{-1} ; right axes). Vectors denote the 20-90-day band-pass filtered wind
966 vectors whose horizontal component is the zonal wind (m s^{-1}), and the vertical component is
967 the pressure velocity (Pa s^{-1} , multiplied by a factor of -100). All values are averaged between
968 5°S - 5°N .

969

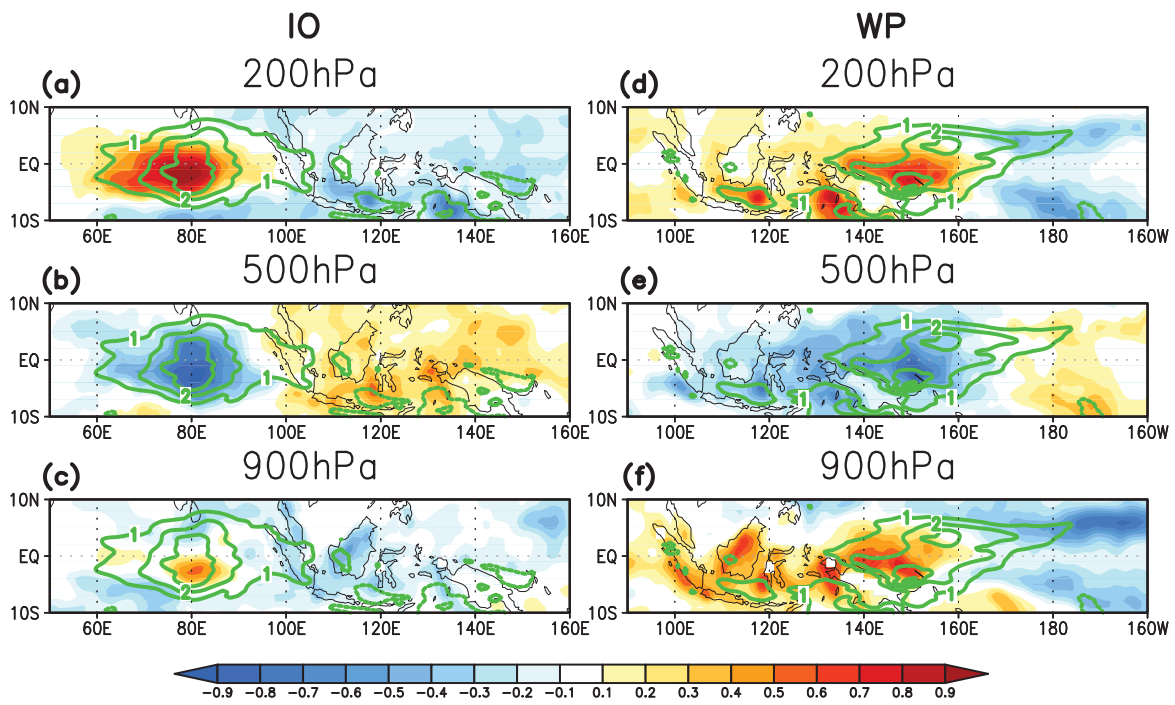
970

971

972

973

974



976

977 Figure 3. Spatial patterns of regressed subgrid-scale momentum tendency (shaded, $\text{m s}^{-1} \text{ day}^{-1}$) at
 978 200hPa (top), 500hPa (middle), and 900hPa (bottom), and 20-90-day filtered precipitation
 979 anomalies (green contour, mm day^{-1}) onto the IO (left) and WP (right) MJO indices.

980

981

982

983

984

985

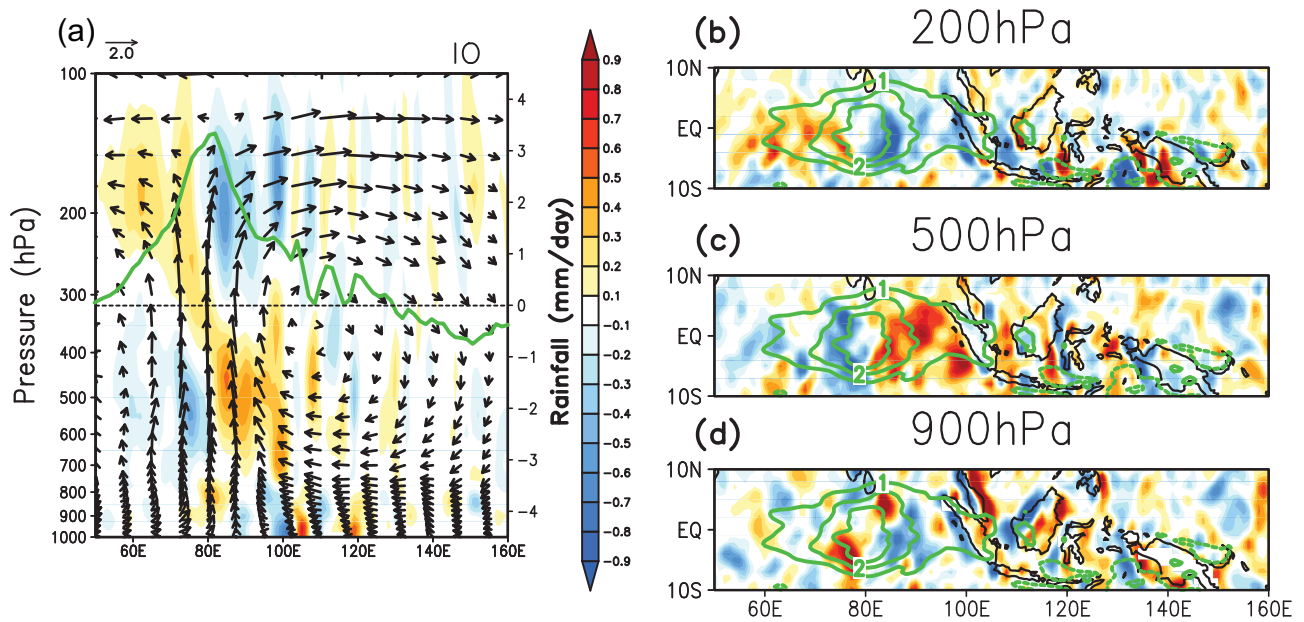
986

987

988

989

990



991

992 Figure 4 (a) Same as Fig. 2a, but for zonal divergence of subgrid momentum tendency (shaded; 10^{-6}
993 $s^{-1} \text{ day}^{-1}$); (b-d): Same as Fig. 3a-c, but with zonal divergence of subgrid CMT for the shaded
994 contours ($10^{-6} s^{-1} \text{ day}^{-1}$).

995

996

997

998

999

1000

1001

1002

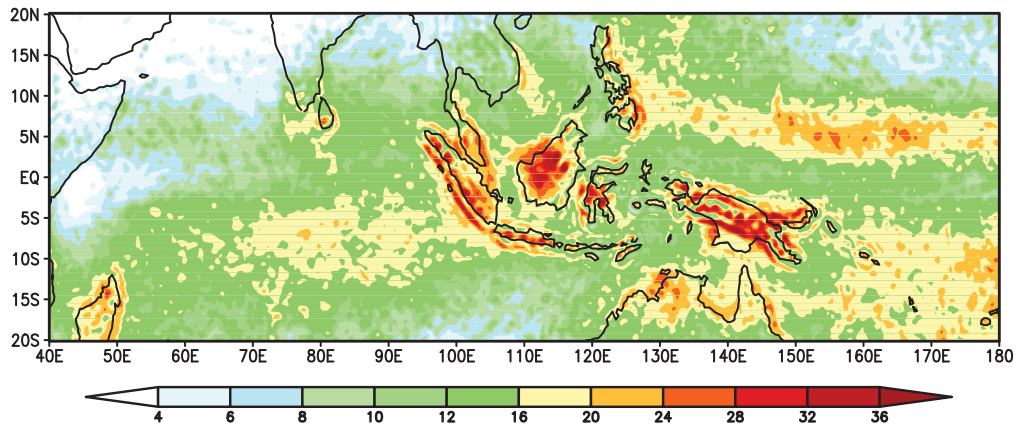
1003

1004

1005

1006

1007



1008

1009 Figure 5 Standard deviation of the mesoscale rain derived by the spatial-scale separation (mm day⁻¹)

1010 based on the CFSR for 12 winters (NDJFMA).

1011

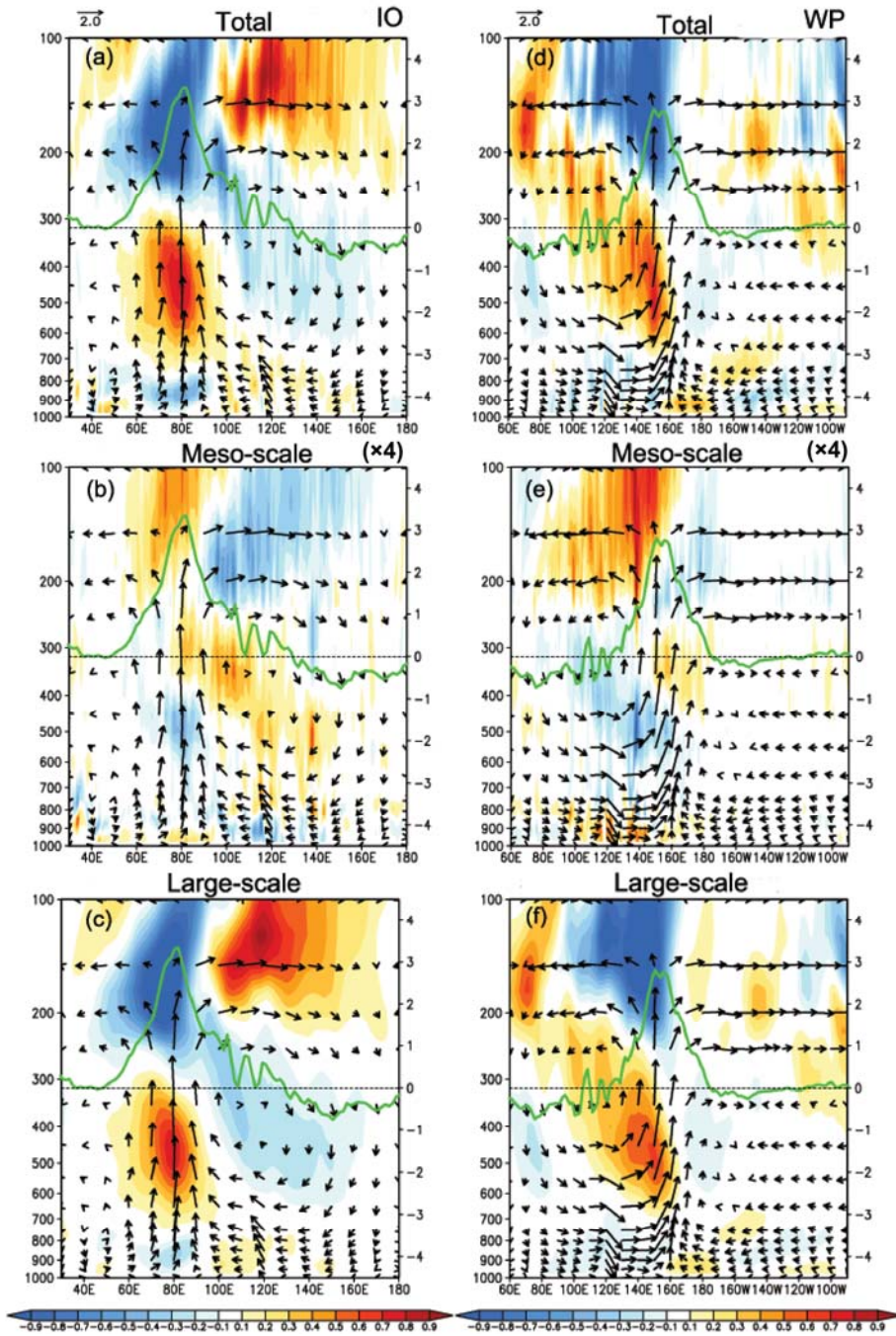
1012

1013

1014

1015

1016



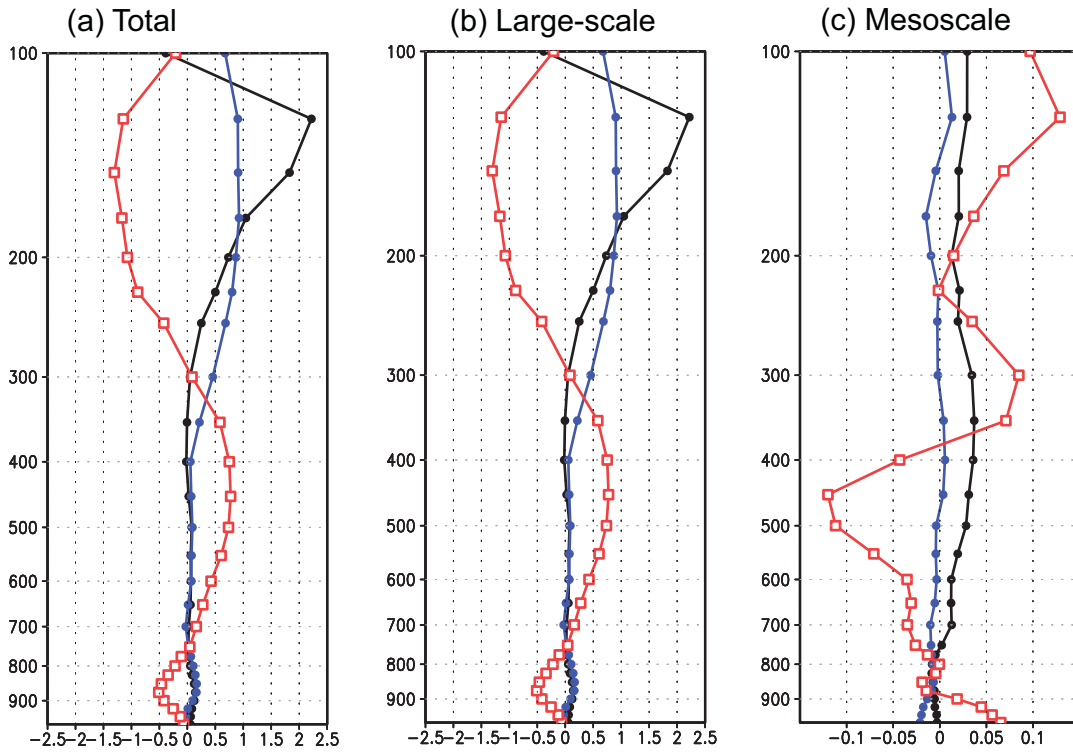
1017

1018 Figure 6 Longitude-height diagrams of $5^{\circ}\text{S}-5^{\circ}\text{N}$ averaged grid-scale u -momentum tendency (m s^{-1}
 1019 day^{-1}) by: (a), (d) total vertical momentum transport, $-\partial(u\bar{\omega})/\partial p$, (b), (e) meso-scale CMT,
 1020 $-\partial(u'\omega')/\partial p$, and (c), (f) large-scale momentum transport, $-\partial(\bar{u}\bar{\omega})/\partial p$ regressed onto MJO
 1021 indices over the IO (a-c), and WP(d-f). For the sake of comparison, $-\partial(u'\omega')/\partial p$ is
 1022 multiplied by a factor of 4. The green lines and vectors are the same as in Fig. 2, denoting
 1023 corresponding regressed rainfall anomalies (mm day^{-1}) and circulations.

1024

1025

1026



1027

1028 Figure 7 Vertical profiles of u-momentum tendencies ($\text{m s}^{-1} \text{ day}^{-1}$) by zonal (black), meridional
1029 (blue), and vertical (red) transports by: (a) total grid-scale; (b) large-scale, and (c) mesoscale
1030 circulations, respectively, based on the regression onto the IO MJO index. Note the different
1031 scale in the x-axis of (c). All variables are averaged over the regions of 75°E - 85°E , 5°S - 5°N .

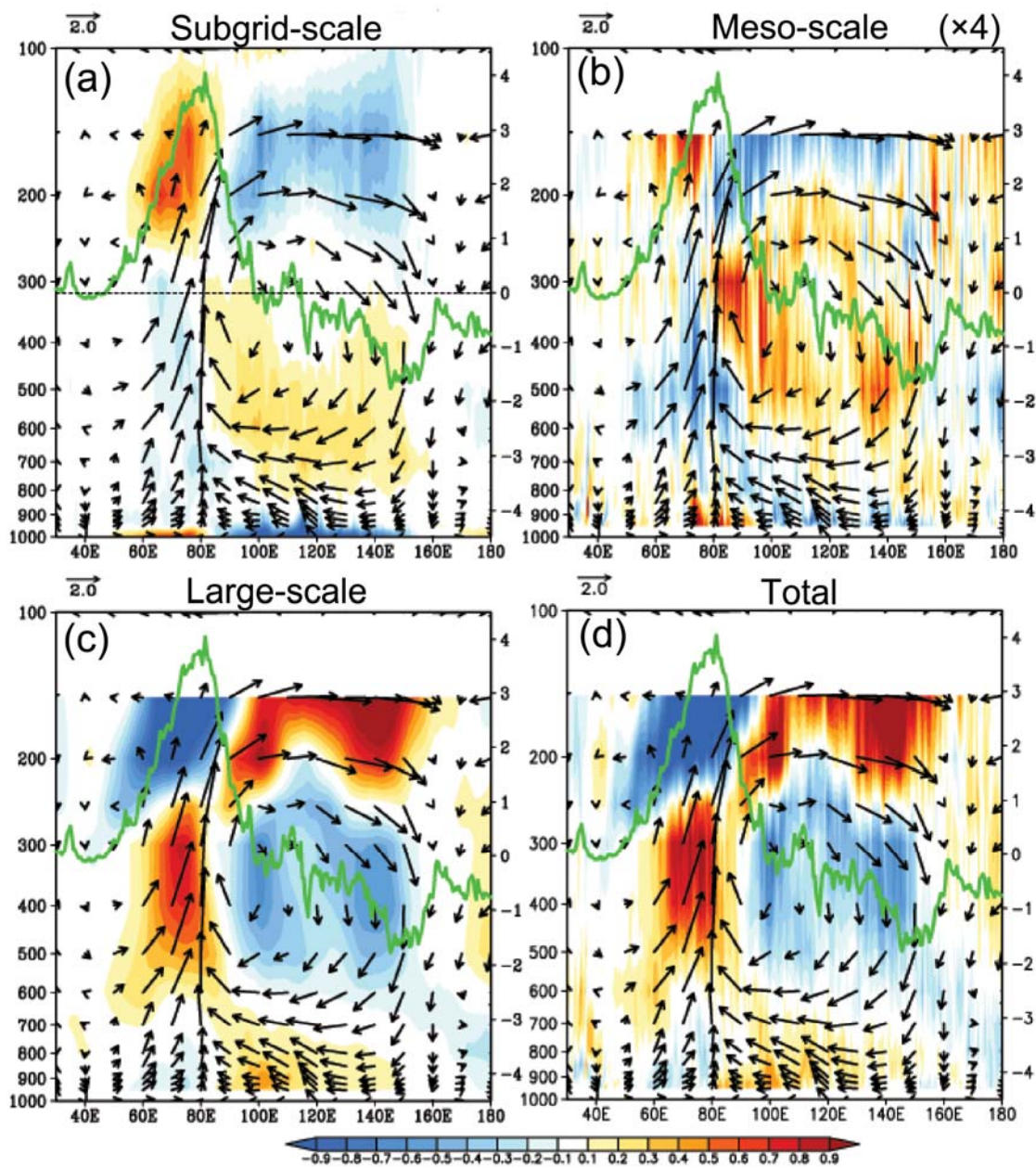
1032

1033

1034

1035

1036



1037

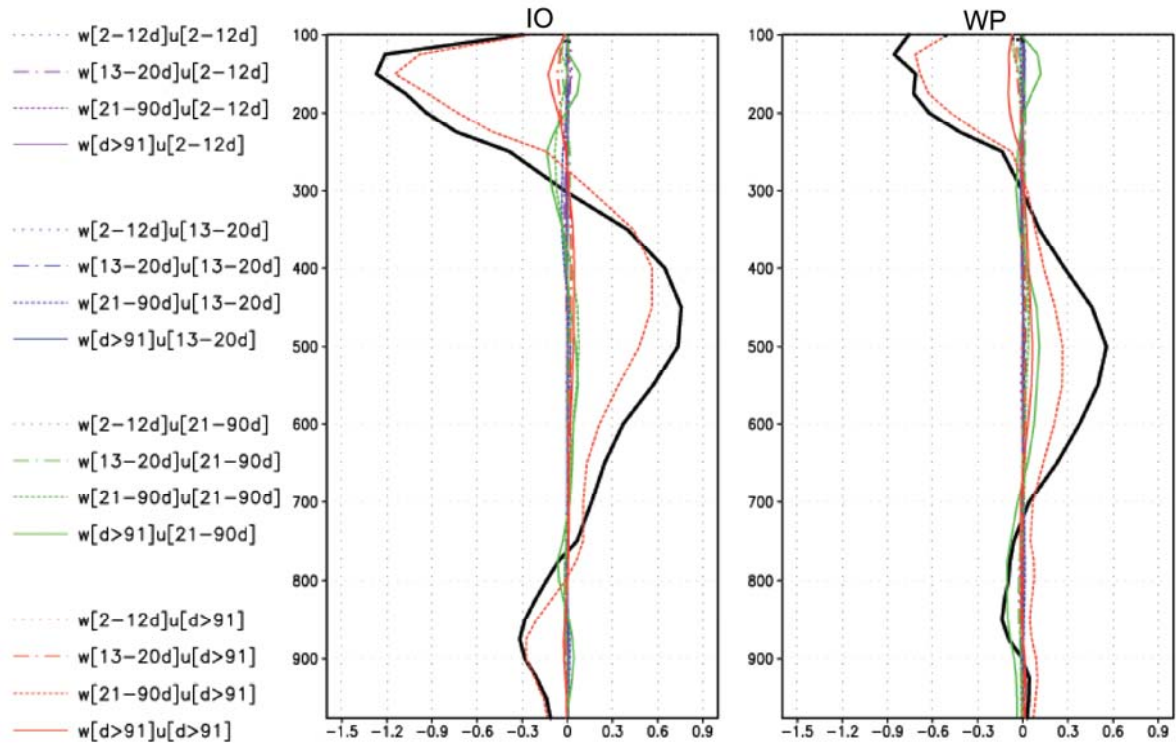
1038 Figure 8 Longitude-height plots of momentum tendency based on the EC-YOTC analysis (shaded,
 1039 units: $\text{m s}^{-1} \text{ day}^{-1}$) by: (a) subgrid-scale, (b) mesoscale, (c) large-scale, and (d) total grid scale
 1040 vertical transports derived by regressions onto the IO MJO index. The mesoscale momentum
 1041 tendency in (b) is multiplied by a factor of 4. The green lines and vectors are the same as in
 1042 Fig. 2 but based on the EC-YOTC analysis. All values are averaged between 5°S - 5°N .

1043

1044

1045

1046



1047

1048

1049 Figure 9 Vertical profiles of large-scale u-momentum tendency ($\text{m s}^{-1} \text{ day}^{-1}$) due to vertical
 1050 transport by circulations on various time scales based on regressions against the IO (a) and
 1051 WP (b) MJO indices. Values are averaged over $75^{\circ}\text{E}-85^{\circ}\text{E}$, $5^{\circ}\text{S}-5^{\circ}\text{N}$ in (a) and $150^{\circ}\text{E}-160^{\circ}\text{E}$,
 1052 $5^{\circ}\text{S}-5^{\circ}\text{N}$ in (b). The black solid lines represent total large-scale vertical transports.

1053

1054

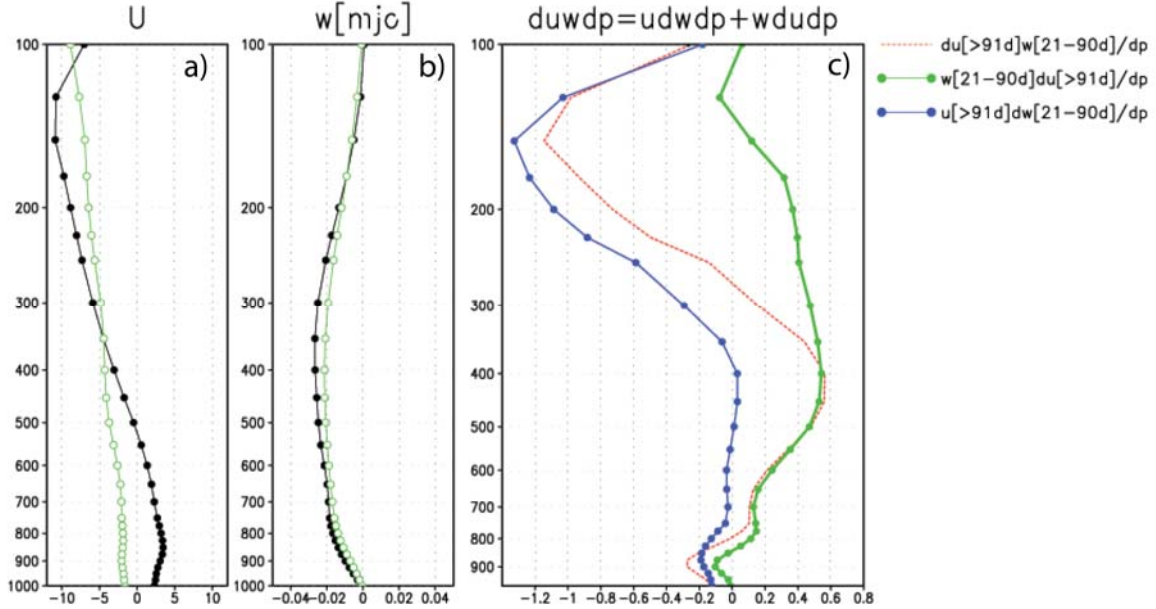
1055

1056

1057

1058

1059



1061

1062

1063 Figure 10 Vertical profiles of (a) winter mean zonal wind (m s^{-1}), (b) 21-90 day band-pass filtered
 1064 vertical pressure velocity (Pa s^{-1}) regressed against the MJO index for the IO ($75^{\circ}\text{E}-85^{\circ}\text{E}$,
 1065 $5^{\circ}\text{S}-5^{\circ}\text{N}$; black) and the WP ($150^{\circ}\text{E}-160^{\circ}\text{E}$, $5^{\circ}\text{S}-5^{\circ}\text{N}$; green); (c): The
 1066 $-\partial([\bar{u}]_{>91d}[\bar{w}]_{21-90d})/\partial p$ term over the IO (red dashed, duplicated from Fig. 9a; units: m s^{-1}
 1067 day^{-1}), and its decomposition into $-\partial([\bar{w}]_{21-90d}[\bar{u}]_{>91d})/\partial p$ (green) and
 1068 $-\partial([\bar{u}]_{>91d}[\bar{w}]_{21-90d})/\partial p$ (blue).

1069

1070

1071

1072

1073

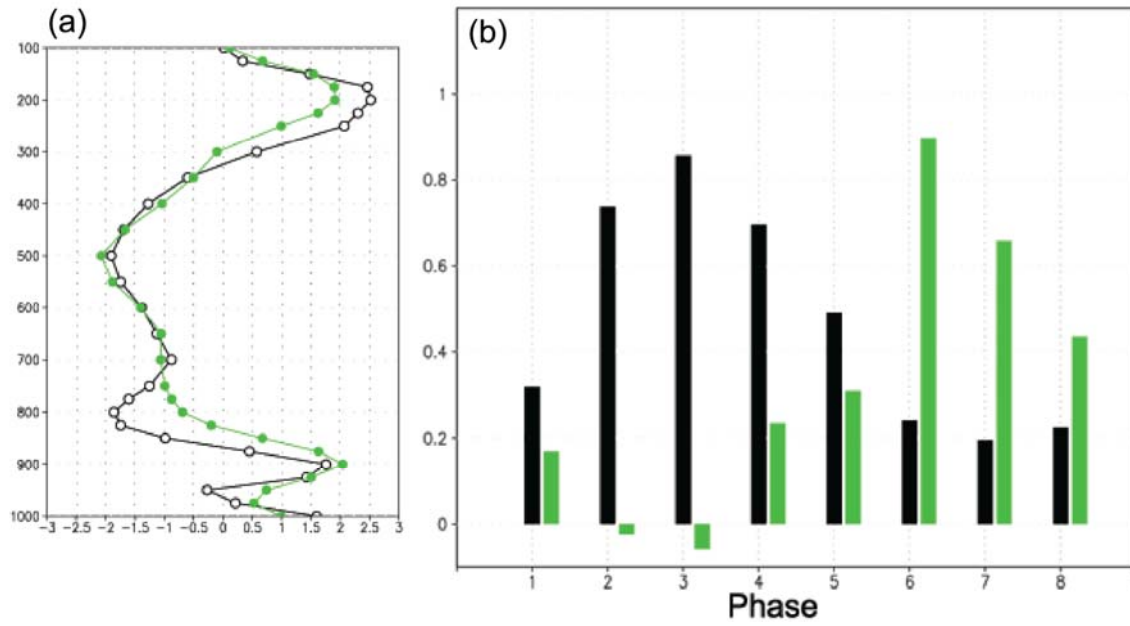
1074

1075

1076

1077

1078



1079

1080 Figure 11 (a) Vertical profiles of the first leading EOF mode of subgrid momentum tendency over
1081 the IO (black) and WP (green); (b) Corresponding composite PC coefficients as a function of
1082 the RMM MJO phases.

1083

1084

1085

1086

1087

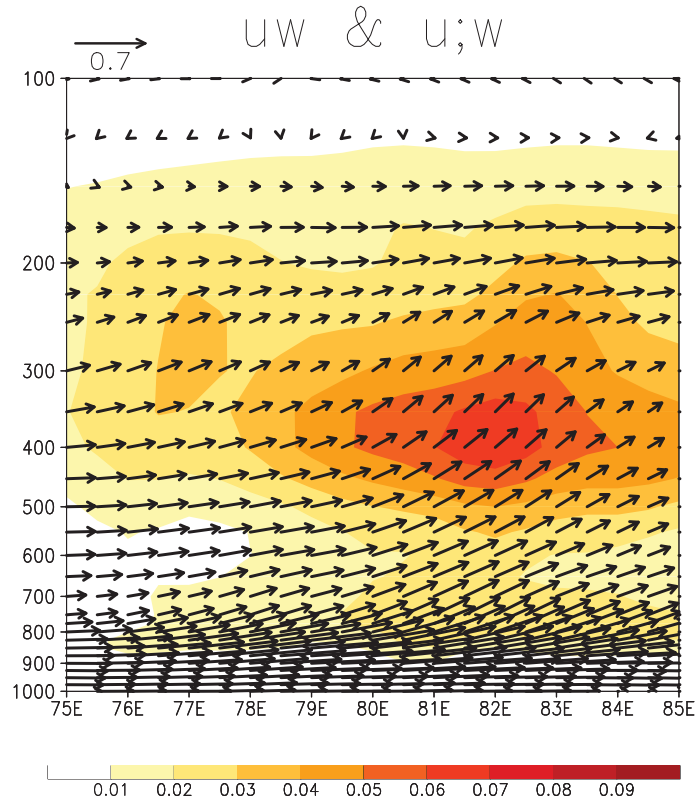
1088

1089

1090

1091

1092



1094

1095 Figure 12 Pressure-longitude profiles of the subgrid-scale CMT ($-u'\omega'$; shaded) and circulation
 1096 (vectors; horizontal for zonal winds u' with units of m s^{-1} and vertical for the pressure velocity
 1097 ω' with units of Pa s^{-1} and multiplied by a factor of -10 for display) derived by regression onto
 1098 the PC time series of the first leading EOF of the subgrid momentum tendency over the IO.

1099

1100

1101